

We are IntechOpen, the world's leading publisher of Open Access books Built by scientists, for scientists

5,800

Open access books available

142,000

International authors and editors

180M

Downloads

Our authors are among the

154

Countries delivered to

TOP 1%

most cited scientists

12.2%

Contributors from top 500 universities



WEB OF SCIENCE™

Selection of our books indexed in the Book Citation Index
in Web of Science™ Core Collection (BKCI)

Interested in publishing with us?
Contact book.department@intechopen.com

Numbers displayed above are based on latest data collected.
For more information visit www.intechopen.com



Influence of Piezoelectric Actuator Properties on Design of Micropump Driving Modules

Matej Možek, Borut Pečar, Drago Resnik and Danilo Vrtačnik

Abstract

The chapter will briefly present three distinctive concepts of the micropump actuator driving module, each with its waveform specifics and their impact on particular micropump performance (pumping media, flow rate and backpressure). First presented concept is based on two mutually-exclusive boost switched-mode power supply modules. Characterization of this module identified output voltage asymmetry to be the limiting factor of micropump performance. To assure driving symmetry, an alternative driving module, based on independent high-voltage stages and optocouplers, was implemented. This design is capable of driving a piezoelectric micropump with a rectangular waveform of programmable frequency, positive and negative amplitudes, slew rates and dead time. While this design provides maximum flow and backpressure characteristics, it does not offer minimal current consumption and long-term operation. To overcome this difficulty, our current design is based on an embedded arbitrary waveform generator, which offers an efficient trade-off between high pumping performance and low current consumption.

Keywords: piezoelectric micropumps, mutually exclusive switched-mode power supply modules, optocoupler, arbitrary waveform generator, low current consumption

1. Introduction

Modern microfluidic applications are moving toward miniaturization and lowering current consumption demands. Consequently, digital system voltages are lowered to a level of 3 V and below, which are most commonly used today. On the other hand, piezoelectric micropumps need a high voltage signal in the range of few hundred volts for normal operation. Driving signal parameters are depending on PZT material (Lead zirconate titanate), construction and required performance of a specific micropump. Therefore, a low-power portable piezoelectric micropump driver presents an interesting challenge in electronics design.

In addition to being capable of high voltage waveform synthesis, the piezoelectric micropump driver should allow for the adaptations of signal waveform shape, amplitude and frequency. These parameters need to be optimized for a type of driven micropump in order to maximize the microfluidic system performance.

Commercially available drivers are often either physically large and therefore non-portable [1] or are dedicated to driving a particular type of piezoelectric

micropump [2]. Furthermore, available drivers offer only limited signal flexibility. In our previous work, a 3-channel high voltage AB class linear amplifier was developed [3]. This module offered very good micropump driving signals up to 10 kHz, but it was not size optimized. A miniaturized, high-voltage micropump driver was also implemented using a piezo haptic driver DRV2667 [4]. This implementation featured fully-programmable signal shape, frequency and amplitude, but was limited by signal driving amplitude to $200 V_{pp}$ and frequency range up to 1 kHz. Current consumption was 134 mA at such high excitation voltages.

The above-listed limitations of referenced drivers encouraged the development of a simpler, cost-effective micropump driver electronic module, which would be limited to a rectangular driving signal, but would offer excitation with higher voltages, whilst maintaining the low-power aspect (i.e. current consumption in the order of tenths of mA). One option was to design the driver with a separate high-voltage power supply, which provides a driving signal using an H-bridge, but due to complexity of such a circuit, this never represented a cost-effective solution. H-bridge topology does not ground one of the micropump actuator terminals.

Low-cost aspect of aforementioned implementations was challenged by a transformerless design, proposed and patented by Fraunhofer IZM [5]. Their brilliantly simple idea features two switched-mode power supply (SMPS) boost converters, which operate in mutual exclusion. Each boost converter forms voltage of either positive/negative polarity, but both SMPS converters incorporate same piezoelectric micropump as its output capacitor. The need for a dedicated output capacitor results in a miniature, digitally controlled version of a piezoelectric micropump driving module. Such interchanging SMPS module design synthesizes rectangular shape of driving signal with resistor-capacitor (RC) charging and discharging transitions through the piezoelectric micropump. Though the resulting edge transitions of a rectangular micropump driving signal are not ideal, the performance of such a circuit can be considered adequate for certain cost- and size-sensitive applications. The primary objective of this chapter is to present the development of three distinctive micropump driving module designs with their impact on piezoelectric micropump electrical and fluidic characteristics.

2. Micropump module, based on mutually exclusive SMPS

The high-voltage section of the analyzed circuit is designed around two boost SMPS power supplies, depicted in **Figure 1**. Each SMPS module provides corresponding positive and negative micropump excitation voltage: Positive voltage SMPS circuit comprises a switching transistor Q_3 , a diode D_2 , while the negative voltage SMPS comprises the switching transistor Q_4 , diode D_1 . If the switching operation between SMPS modules is alternated repeatedly, a rectangular shape of driving signal with RC charging and discharging transitions is synthesized. Micropump PZT actuator is represented by C_1 and acts as a shared SMPS output capacitor in both circuits. Boost inductance L_1 is also shared. While the driver is supplying negative voltage to the micropump C_1 , the transistor Q_3 is fully open (its base is tied via R_3 to V_{CC}) and the Q_4 with diode D_1 performs the PWM (pulse width modulation) switching. For positive voltage, the roles of Q_3 and Q_4 are reversed: Q_4 is fully open (its base tied via R_4 to GND) and the Q_3 with diode D_2 performs the PWM switching. Transistors Q_1 and Q_2 in common-base orientation provide isolation between the two SMPS stages and prevent micropump capacitor C_1 discharge through the inactive (i.e. fully open) transistor. During positive voltage switching, the Q_4 is fully open - its collector-emitter voltage is reduced to its saturation

.lib <http://twiki.org/files/LTspiceIV/vendor%20List/Zetex/ztx757.lib>
 .lib <http://twiki.org/files/LTspiceIV/vendor%20List/Zetex/ztx657.lib>
 .lib http://www.onsemi.com/pub_link/Collateral/1N4007.REV0.LIB

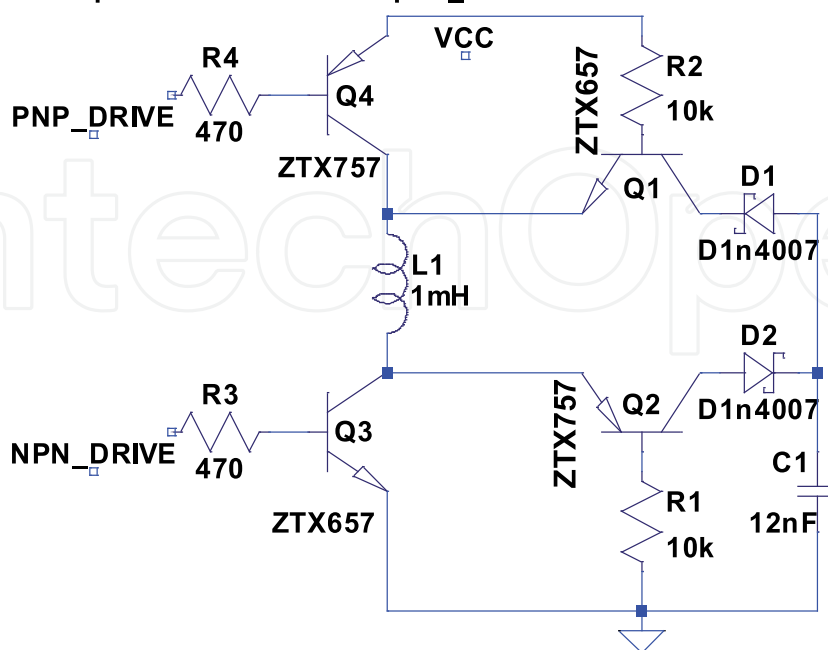


Figure 1.
 High-voltage part of the mutually exclusive SMPS driver design.

value, hence the Q_1 isolation transistor is closed, thus effectively preventing any reverse current flow through diode D_1 . Similar analysis can be applied for transistors Q_2 , Q_3 and the diode D_2 during negative voltage switching cycle.

In order to synthesize a rectangular shape of driving signal with resistor-capacitor charging and discharging transitions, both positive and negative SMPS boost circuits have to be switched in the abovementioned sequence by providing the PNP_DRIVE and NPN_DRIVE signals.

To achieve this, an initial, simplified version of the micropump driving circuit was designed to assess the optimal PWM switching frequency range and establish the need for a PWM drive. High voltage part driving circuit, depicted in **Figure 2**, was based around a TTL 74HC257 4-channel 2/1 multiplexer for 5 V power supply version or its CMOS counterpart (40257) for 12 V version. Each 2/1 multiplexer comprises a and b inputs and an output Y . All multiplexers share the same selection input s . In **Figure 2**, only lower two multiplexers, indexed 0 and 1, are used. High-frequency switching is provided by 2 AC voltage sources V_2 and V_4 . Micropump excitation frequency signal is provided by V_3 , which is connected to the multiplexer selection input. Toggling speed of the multiplexer selection input thus corresponds to mutual exclusion of SMPS power supplies, which directly translate to micropump excitation frequency.

2.1 Circuit simulations

Above described circuit was initially simulated using LTSpice IV [6]. In presented case micropump was modeled using previously measured capacitance C_0 of 12 nF [7]. Synthesized rectangular signal frequency, which represents micropump excitation, was set at 100 Hz with 50% symmetry. High-frequency switching of transistors Q_3 and Q_4 was swept from 10 kHz to 33 kHz, whilst recording resulting micropump excitation voltage. Resulting recorded micropump voltage at 100 Hz is depicted in **Figure 3**.

.lib <http://ltw iki.org/files/L TspiceIV/Vendor%20List/Zetex/ztx757.lib>
 .lib <http://ltw iki.org/files/L TspiceIV/Vendor%20List/Zetex/ztx657.lib>
 .lib http://www.onsemi.com/pub_link/Collateral/1N4007.REV0.LIB
 74 hct and dview libraries : <http://www.spot.pcc.edu/~ghecht/L Tspice.html>
 .lib 74hct.lib .lib dview.lib

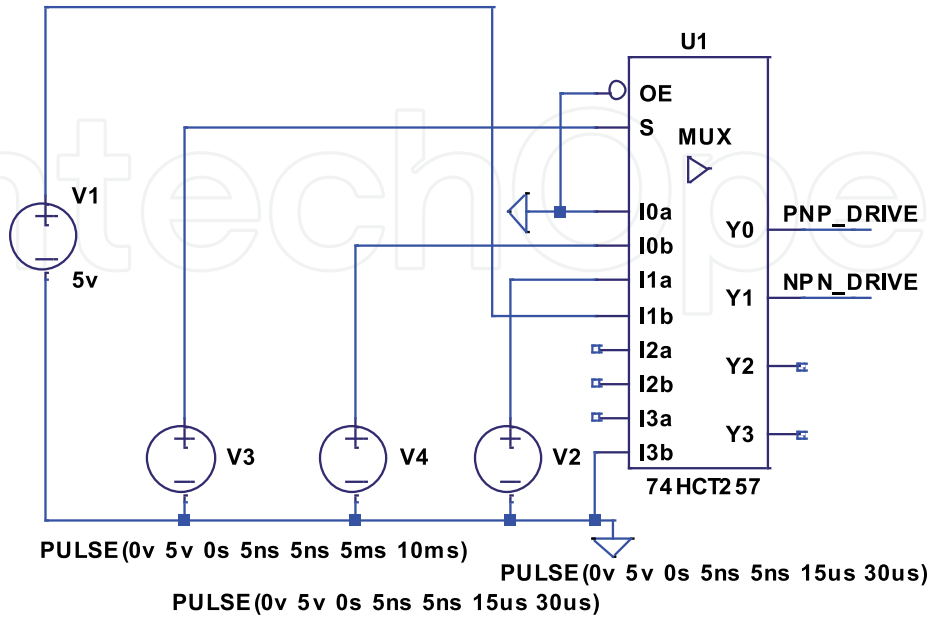


Figure 2.
 Excitation part of the mutually exclusive SMPS driver design.

Initial simulations have shown, that the output voltage, depicted in **Figure 3**, features a pronounced, unwanted asymmetry of positive and negative half-cycle amplitudes in order of 50 V. This consequentially causes a DC offset voltage, which deteriorates the piezo actuator deflection over time or even prevents proper micro-pump performance.

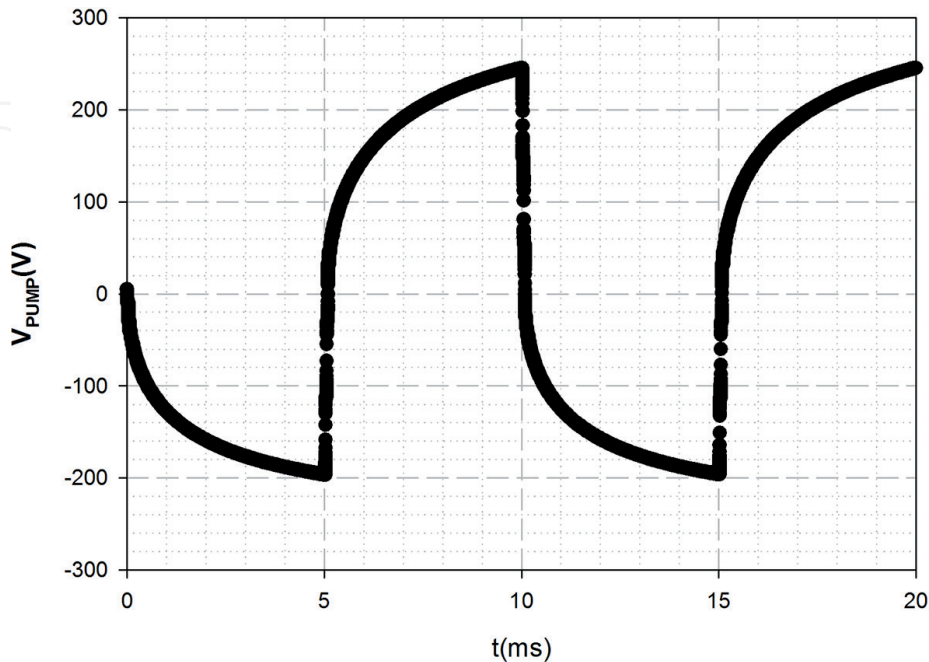


Figure 3.
 Micropump excitation voltage simulation.

This discrepancy between positive and negative excitation voltage can be roughly adjusted using different base resistors R_3 and R_4 . On the other hand, micropump drivers must be able to independently set the amplitude of micropump excitation signal during positive and negative half-cycle. Analyzed high-voltage circuit, presented in **Figure 1**, does not have such ability. However, due to simple high-voltage circuit topology, the possibility of individual half-cycle amplitude setting was investigated further.

2.2 Large-scale prototype

A large-scale prototype, depicted in **Figure 4**, was designed and implemented. This design was based on through-hole elements for purpose of verification of simulated circuits and selection of appropriate switching transistors.

Switching transistors, which were used during simulations (ZTX657/757), were not available in surface mount housing, therefore other complementary high-voltage bipolar transistors FMMT458/FMMT558 were tested. Better transistor-to-transistor matching and hence better DC offset control was achieved using PBHV9040/PBHV8540 pair of transistors. A test setup, comprised of three Agilent 33120B arbitrary waveform generators and a Siglent SDS1102X oscilloscope was connected to initial prototype: First Agilent 33120B generated micropump operation frequency by supplying square-wave signal to the 40,257 multiplexer, while the other two generators provided square-wave PWM modulated frequencies for high switching frequency excitation of corresponding transistor Q_3/Q_4 (refer to **Figure 1**). Synthesized driving signal frequency was set from 100 Hz to 400 Hz in 100 Hz steps. At each micropump frequency setting, high-switching frequency and duty-cycle were altered with aim to determine output voltage peak-to-peak maximum, whilst maintaining the minimum of DC offset. After each completed micropump frequency sweep, power supply voltage was altered (5 V, 10 V and 12 V). Resulting excitation signal frequency scan vs. micropump amplitude is depicted in **Figure 5**. Amplitude values were very promising, especially in the upper-frequency range (i.e. 400 Hz), where amplitudes up to 240

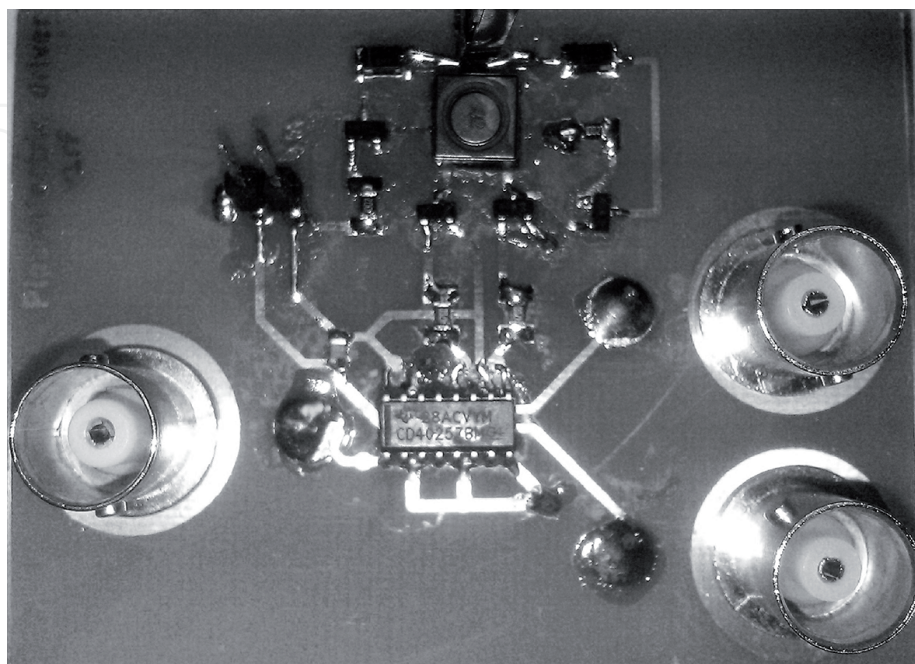


Figure 4.
Large-scale driver prototype (mutually exclusive SMPS).

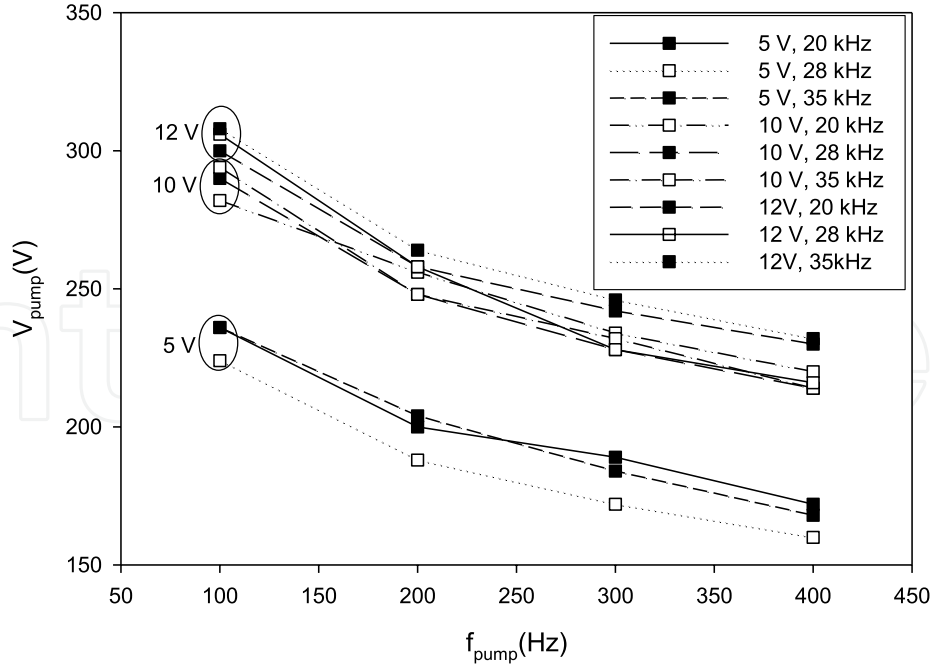


Figure 5.
Frequency sweep of the initial prototype.

V_{pp} were achieved with 12 V power supply voltage. In addition, **Figure 5** shows the boundaries of application range in terms of power supply voltage and high-switching frequency for micropumps, developed in our laboratory [7].

PWM duty cycles of Q_3 and Q_4 transistors, referred to as D_{Q_4} and D_{Q_3} , which provide maximal micropump amplitude values in **Figure 5**, are summarized in **Tables 1** and **2**. The values are referring to an active part of duty cycle, where a certain transistor is open (i.e. NPN_DRIVE set to V_{CC} , PNP_DRIVE set to GND).

Values, listed in **Tables 1** and **2**, were used in software as pre-programmed duty-cycles, which yield symmetrical positive and negative amplitude of micropump driving signal.

2.3 Module optimization

After assessment of large-scale prototype measurements, presented in **Figure 5**, the true complexity of Q_3 and Q_4 transistors driving signals were revealed—although the circuit operation in **Figure 1** may appear simple, it needs a fairly complex excitation. In order to balance out positive and negative half-period amplitudes in terms of

f _{PWM} (Hz)	20 kHz		28 kHz		35 kHz	
f(Hz)	D _{Q4}	D _{Q3}	D _{Q4}	D _{Q3}	D _{Q4}	D _{Q3}
100	41%	58%	23%	73%	34%	51%
200	40%	62%	26%	73%	41%	56%
300	39%	62%	29%	73%	37%	59%
400	42%	69%	32%	73%	33%	63%

Table 1.
PWM duty cycles (%) for Q_3/Q_4 transistors @ $V_{CC} = 5$ V.

$f_{\text{PWM}}(\text{Hz})$	20 kHz		28 kHz		35 kHz	
$f(\text{Hz})$	D_{Q4}	D_{Q3}	D_{Q4}	D_{Q3}	D_{Q4}	D_{Q3}
100	9%	93%	8%	93%	9%	91%
200	9%	94%	10%	94%	9%	93%
300	9%	94%	11%	95%	7%	93%
400	6%	94%	10%	95%	7%	93%

Table 2.
 PWM duty cycles (%) for Q3/Q4 transistors @ $V_{\text{CC}} = 12 \text{ V}$.

DC offset, a single, switched PWM generator, with a switching frequency in order of 30 kHz with at least 7-bit PWM resolution had to be implemented as a cost-effective solution. Micropump output voltage should be monitored and included in closed-loop regulation with adjustment of duty cycle to minimize the driving signal DC offset.

The above-listed requirements would preferably have to be implemented in software, using an 8-bit microcontroller. In our cost-effective implementation, depicted in **Figure 6**, a Microchip ATtiny10 [8], was selected for its price and availability in a 6-pin SOT-23 package. In order to extend the module power supply operating range to 18 V, the microcontroller is connected to a non-inverting, 2-channel MOSFET driver TC4427, which also acts as a voltage level translator for driving signals NPN_DRIVE and PNP_DRIVE (refer to **Figure 1**). Driver inputs are 5 V compatible, therefore the microcontroller can operate at a 3.3 V power supply, thus keeping total current consumption at a minimum, which is a prerequisite for

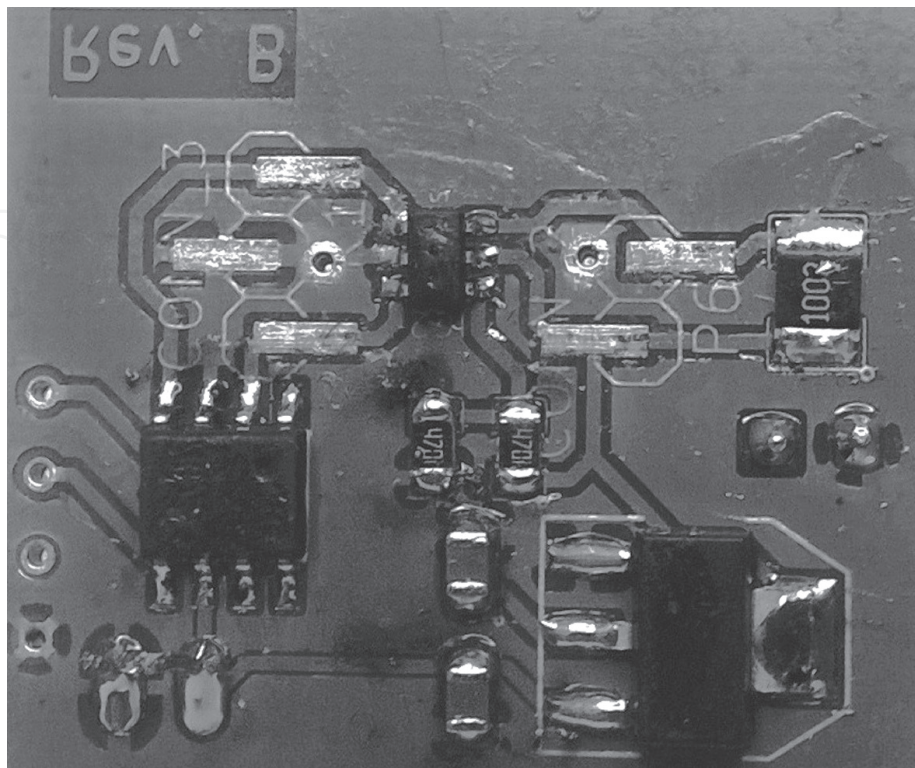


Figure 6.
 Miniaturized driver based on microcontroller ATtiny10.

autonomous (e.g. battery-powered) application. Low voltage 3.3 V microcontroller power supply was generated using LM1117–3.3 circuit.

In order to provide driving signals for Q_3/Q_4 transistors, an 8-bit PWM unit zero in ATtiny10 with two output compare channels (A and B) was used in phase non-aligned mode. Compare value of PWM channel A and B was set using dedicated output compare registers OC0A/OC0B, respectively. Interrupt, which can be triggered upon output compare match with corresponding compare register (OC0A/OC0B), was not used. Instead, each PWM channel toggles between a switching (PWM) state and an inactive (fully open) state. Switching between both states, previously achieved with a '257 multiplexer, can be implemented without additional components, by switching the corresponding pin mode from PWM state (i.e. OC0x mode) to normal I/O state (i.e. PORTB I/O mode).

Achieving switching frequencies in the range of 30 kHz with 8-bit resolution requires the internal oscillator to be configured at 8 MHz. Using such an internal clock signal with no prescaling on timer TMR0 synthesizes a 31.25 kHz PWM clock. Resulting PWM unit features an 8-bit resolution.

Micropump excitation frequency was determined by counting TMR0 timer overflows. As the number of overflows reaches a predefined value, the Q_3/Q_4 transistors excitation roles are reversed by toggling the PWM pin mode and resetting the overflow counter. All this was accommodated inside interrupt routines, without the need for a complex program. In order to compensate for supply voltage variations, the microcontroller also features an analogue-to-digital (A/D) converter, which is used for module power supply measurement. Using A/D readout, PWM driving frequency and both duty cycles were adjusted according to the values, predefined in a software table, derived from **Tables 1** and **2**. This table also encompasses over- and under-power supply voltage detection, which causes the module to turn both Q_3 and Q_4 outputs off. Presented approach implements an open-loop control, which adjusts the duty cycle value according to the power supply voltage.

2.4 Electrical and fluidic characterization

Previously presented optimized module was tested for current consumption and output signal accuracy with different capacitive loads connected to the output. A multimeter on the power supply line was used to measure current consumption and an oscilloscope was used to measure output signal parameters (waveform shape, amplitude symmetry, frequency). High voltage variable capacitor with values from 10 nF to 100 nF and several piezoelectric micropumps in parallel were used to vary the capacitance of output load. A constant micropump operation frequency was set at 190 Hz, while the power supply voltage was set to 9 V.

Though the resulting capacitance driving capability in **Figure 7** exhibits practically linear dependency, it must be emphasized, that the signal shape deteriorates severely and the positive signal slew rate drops from 140 V/ms range to 80 V/ms.

Measured limiting value of load capacitance, which maintains 140 V/ms slew rate was found at 57 nF with a driving voltage of 172 V_{pp}. Larger capacitive loads (> 57 nF) cause the micropump driver current to saturate, which deteriorates the output signal rise- and fall-time and correspondingly the slew-rate. This reduction consequentially results in a drastic deterioration of micropump flow and backpressure characteristics. Such output signal deterioration was attributed primarily to limited current passing through the inductor L_1 .

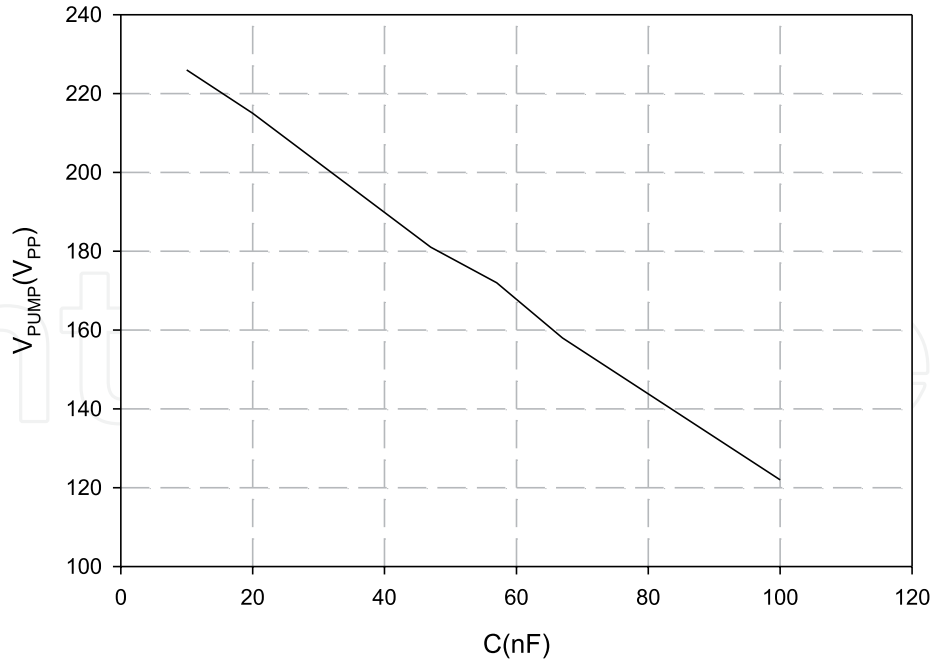


Figure 7.
 Micropump driving voltage vs. variable load capacitance.

In order to achieve better signal integrity, peak L_1 inductor current should be increased—which is in contradiction with low-power design aspect. Due to unavailability of higher-quality inductors, all our designs used a Bourns SRR0603-102KL inductor [].

Figure 8 represents measured results of output signal with 12 nF capacitive loading, achieving 236 V_{PP} drive amplitude, with positive and negative slew rates 142 V/ms and 163 V/ms, respectively. Positive cycle amplitude was 122 V, while the negative was -114 V.

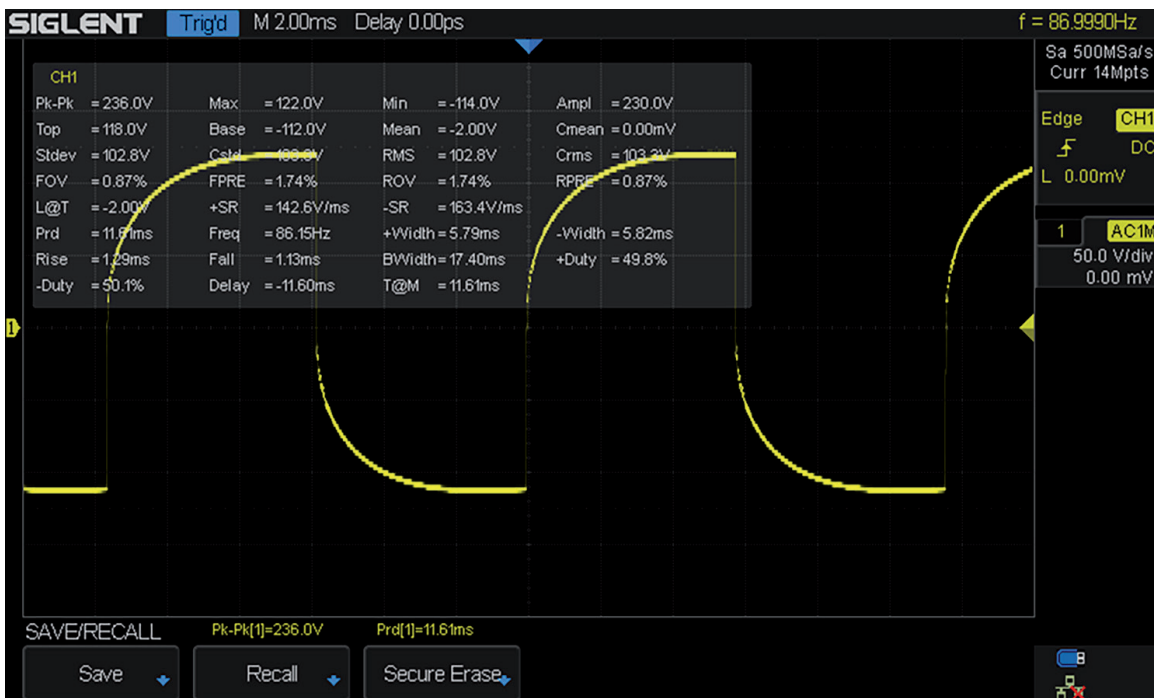


Figure 8.
 Micropump driving voltage at 87 Hz.

Afterwards, the module current consumption was measured after performing a sweep of power supply voltages.

Driver current consumption vs. power supply voltage is depicted in **Figure 9**. Module current consumption increases linearly with respect to increasing load and signal frequency up to 55 mA at 12 V power supply, which was the upper design interval

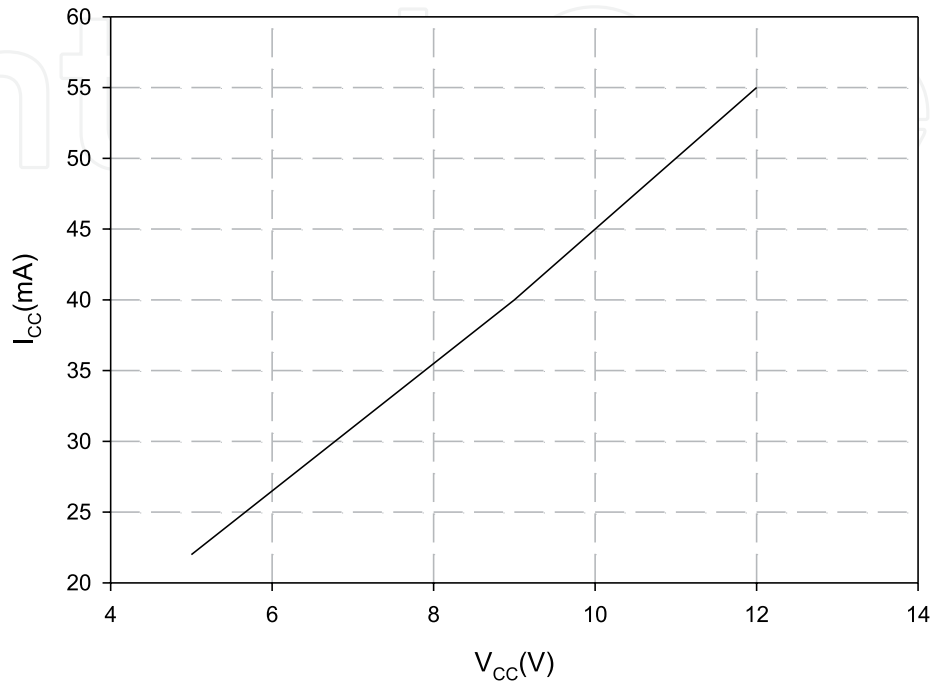


Figure 9.
Driver current consumption.

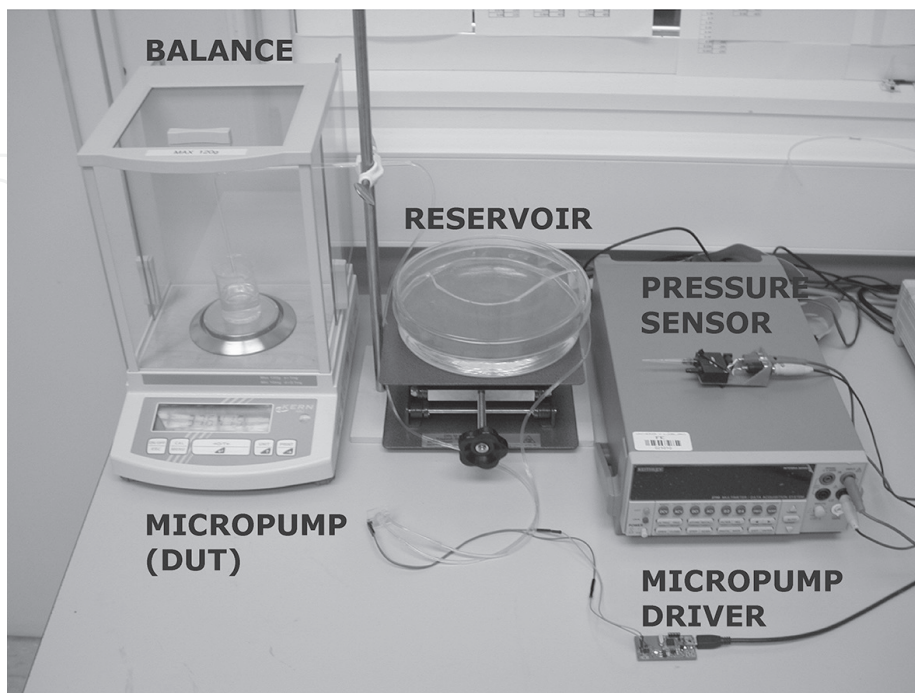


Figure 10.
Measurement setup for micropump fluidic characterization.

limit and also the power dissipation limit of the driver TC4427. Microcontroller current consumption remains negligible throughout entire measurement range. Measured driver current consumption was found between 22 mA (5 V_{CC}) and 55 mA (12 V_{CC}).

A dedicated computer-controlled system for characterization of piezoelectric micropumps was set up after electrical evaluation of the optimized micropump driver. The measurement system, presented in **Figure 10**, enables frequency scans and allows simultaneous pressure and flow measurements.

Analyzed micropump driver was connected to a micropump, developed in our laboratory [7]. A reservoir, filled with DI water, was connected to the micropump input and pressure/flow evaluation equipment on its output.

Micropump flow was measured indirectly by weighing the mass of pumped media over a known period of time using a Kern ABJ 120–4M precision scale. Obtained results were corrected to account for the evaporation of medium during the measurement, which was determined in separate experiments.

Flow measurements are presented in **Figure 11**. Results show frequency scan with comparison to Bartels mp-x Controller [1], which was preset with the same amplitude and frequency conditions. The only difference in driving parameters was the signal shape, where the Bartels mp-x Controller was set to square-wave signal, and the tested driver provided RC like shape, presented in **Figure 8**. The same micropump was driven on a frequency interval from 50 Hz to 400 Hz and both duty cycles were set according to values in **Tables 1** and **2** to achieve minimal DC offset of drive voltage.

Figure 12 summarizes obtained both positive (SR⁺) and negative (SR⁻) slew-rates as well as micropump driving voltage amplitude (not peak-to-peak) with respect to frequency.

For lower frequency range (i.e. under 80 Hz), designed driver actually supersedes the flow performance of Bartels mp-x controller, achieving 1.2 ml/min in comparison to 0.8 ml/min obtained with mp-x module. However, as the driving frequency increases, the slew rate and drive amplitude decrease, resulting in a steady exponential decay of flow performance. As can be observed from **Figures 11** and **12**, best flow

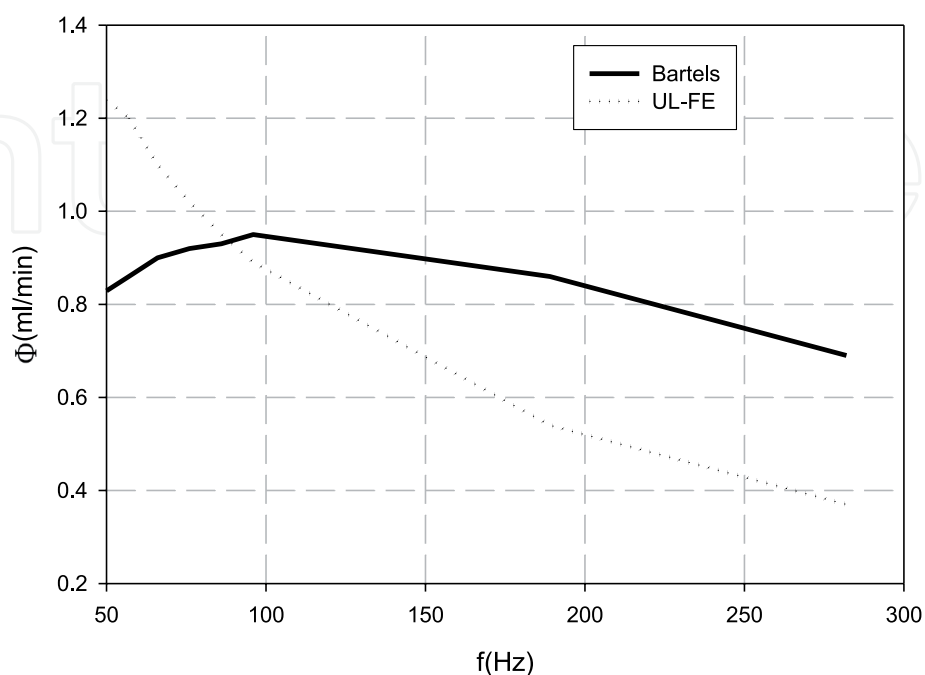


Figure 11.
Micropump DI water flow rate vs. frequency.

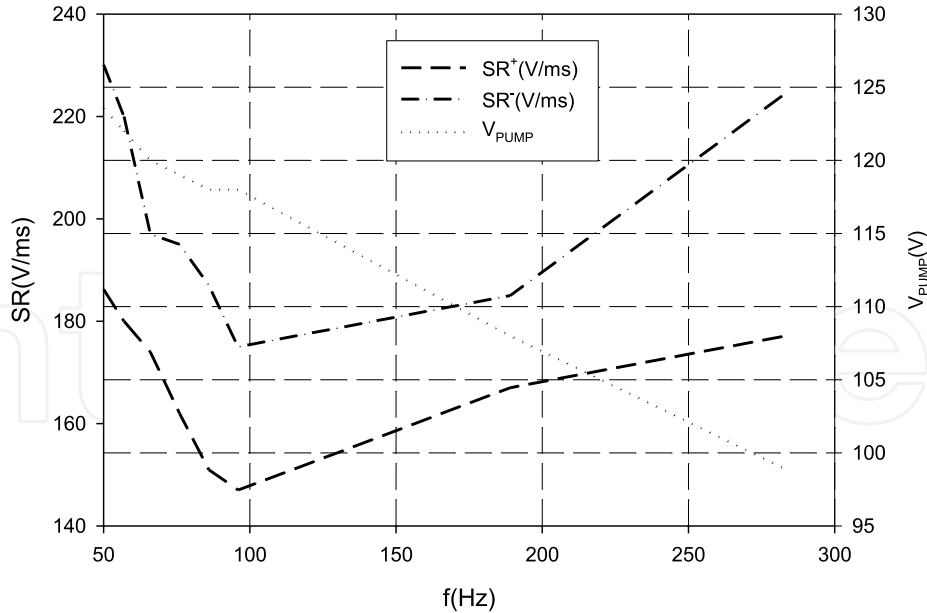


Figure 12.
Slew rate/drive amplitude vs. frequency.

performance of the designed driver is achieved at low frequencies (< 80 Hz), where it is primarily limited by driving voltage amplitude V_{PUMP} and both slew-rates SR^+ and SR^- , depicted in **Figure 12**.

2.5 Influence of excitation signal asymmetry on micropump performance

It is generally accepted, that the shape of the driving signal affects the operation of micropumps. Typically, sine- or square-wave micropump driving signals with symmetric positive and negative amplitudes are most often applied [9–12].

In order to investigate the effect of amplitude asymmetry on micropump performance, driving signals of various amplitude asymmetries had to be synthesized. Since the synthesized signal amplitude depends not only on the output load impedance but also on the duration of each half-cycle by extending the time of first and shortening the time of the second half-cycle, the synthesized signal amplitudes increase and decrease, respectively. In other words, if one boost converter has more time available than the other, it will build up comparatively higher voltage on piezoelectric actuator. The time of both half-cycles is defined by a duty cycle setting. This parameter can be arbitrarily set due to the flexibility of the built-in microcontroller.

We introduced a unique approach, which employs an adjustment of the duty cycle ranging from 30–70%, enabled synthesis of excitation signals with various degrees of amplitude asymmetry, needed for elastomeric micropumps flowrate and backpressure performance characterization. The degree of signal asymmetry is defined as $S_{\text{ASIM}} = V^+ - V^-$. Synthesized signal for four representative duty cycle settings ($DC^+ = 30\%$, 40%, 50% and 60%) and for the duration of 22 ms when driving piezoelectric actuator P-5H (Sunnytec Suzhou Electronics Co., Ltd. [13]) is shown in **Figure 13**. When the duty cycle was set to $DC^+ = 30\%$, the positive amplitude V^+ was lower than the negative amplitude in spite of higher signal slew rate in the first half-cycle. At duty cycle, $DC^+ = 40\%$ amplitude symmetry of driving signal is reached. The maximal value of the applied electric field is 600 V/mm.

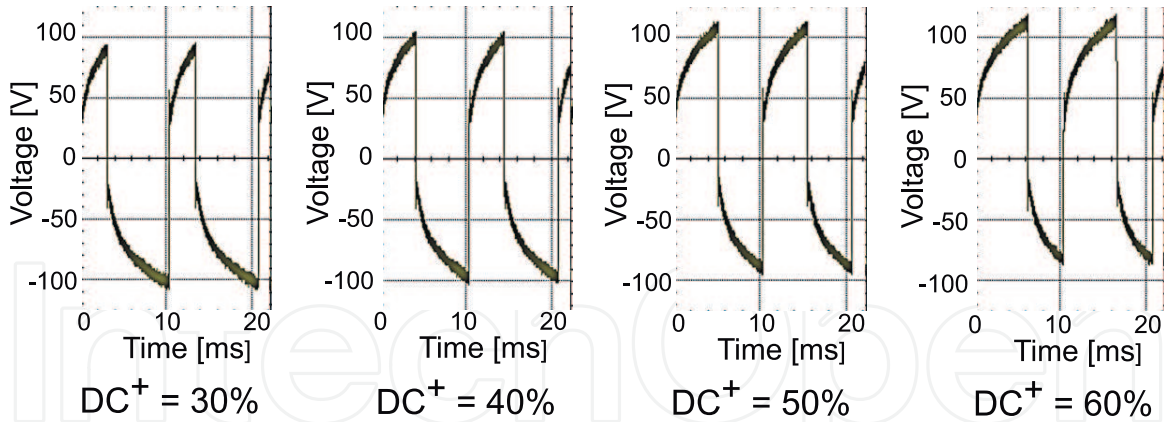


Figure 13. Synthesized excitation signal for four representative values of duty cycle for the duration of 22 ms.

Figure 14 shows micropump [14] flowrate and backpressure performance characteristics vs. excitation signal duty cycle ranging from 30 to 70% at a constant excitation frequency of 100 Hz. Module power supply voltage was set to 9 V.

Excitation signal amplitudes V^+ and V^- , flowrate and backpressure performance for DI water medium were measured for each of the duty cycle setting using the measurement setup, described in **Figure 10**. By extending the DC^+ duty cycle, the amplitude of the positive half-cycle increases while the negative one decreases. The characteristics are similar to linear functions with opposite slopes $+0.43 \text{ V}\%^{-1}$ and $-0.43 \text{ V}\%^{-1}$. Measured characteristics show that flowrate and backpressure performance values are the highest at the duty cycle of equalization DC_{eq}^+ , which is 40%. We assume that in this setting, the efficiency of the suction stroke most probably equals the efficiency of the compression stroke.

By extending the DC^+ duty cycle beyond 40%, the excitation signal amplitude V^+ during micropump compression stroke increases and the amplitude V^- during the suction stroke decreases.

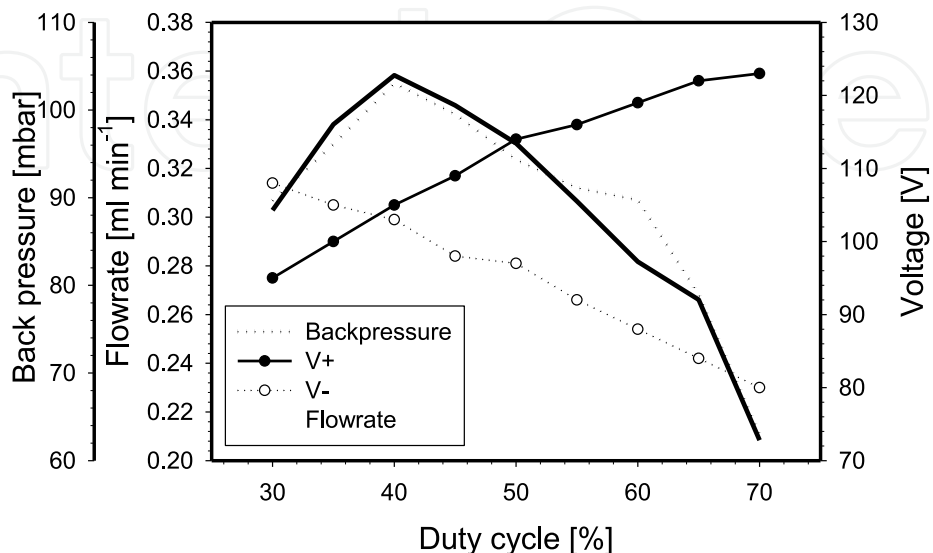


Figure 14. Micropump flowrate and backpressure performance characteristics vs. excitation signal duty cycle ranging from 30 to 70% at a constant excitation frequency of 100 Hz.

Remarkably, the comparatively higher excitation signal amplitude V^+ in the compression stroke fails to compensate for the decrease in the amplitude V^- in the suction stroke and the pumping performance declines. The same trend of performance decline is observed when duty cycle DC^+ is set below 40%. The higher excitation signal amplitude V^- in the micropump suction stroke cannot compensate for the decrease in the amplitude V^+ in the compression stroke and the pumping performance declines again.

Flowrate and backpressure performance of micropump for DI water decreases rather exponentially with increasing degree of signal asymmetry. Based on these characteristics results, it is presumed that the suction and compression stroke performance must be balanced for the highest micropump flowrate and backpressure performance. Hence, the total performance of the pump might only be as high as is dictated by the performance of less efficient stroke. This exponential decrease of pumping performance vs. increasing degree of signal asymmetry coincides with the exponential increase of the pumping performance vs. increasing excitation signal amplitude [15]. Above mentioned exponential trend results from employed active rectifying elements (sequential expansion and throttling of rectifying elements are performed by actuated membrane deformation). If the excitation signal amplitude is reduced, micropump membrane deformation decreases. On the other hand, micropump displacement volume and active rectifying elements efficiency are reduced also.

For micropumps employing passive check valves (sequential opening and closing of check valves are performed by fluidic flow), flowrate and backpressure performance vs. excitation signal amplitude are linear [15]. As the excitation signal amplitude decreases, the displacement volume of micropump decreases, while the efficiency of the passive check valves remains constant. It is speculated that the flowrate and backpressure performance of micropumps employing passive check valves would decrease proportionally with the degree of excitation signal asymmetry S_{ASIM} . It was shown, that micropump flowrate and backpressure performance is limited by a lower amplitude when driven by amplitude-asymmetric signal and that for maximum micropump performance the amplitude symmetric signal is required. Indeed, the performance degradation due to excitation signal asymmetry might be compensated by increasing both the negative and positive half-cycle voltage V^- and V^+ e.g. by increasing the controller's power supply voltage. However, with such an approach, the maximum permissible electric field in the piezoelectric actuator would be exceeded, which equals only 490 V/mm for the PZT-5H standard composition [13]. This would result in permanent actuator performance degradation due to depolarization effect. From measured results (**Figure 14**), it can be concluded that micropumps should be driven by an amplitude-symmetric excitation signal. Therefore, it is mandatory to introduce a solution for providing amplitude symmetry to ensure stable long-term micropump operation and high backpressure and flowrate performance characteristics.

2.6 Impact of excitation signal amplitude symmetry on micropump performance

To compensate for the influence of piezoelectric load and to balance the signal, we introduced a solution based on fine-tuning of duty cycle setting. By prolonging the time of first and shortening the time of the second half-cycle, an amplitude-symmetric signal can be synthesized despite piezoelectric load. The effectiveness of the solution was demonstrated on PZT sample P-5H. The microcontroller code for module was modified to enable adjustment of 16 different signal/pause signal ratios from 20 to 80% in the frequency range from 90 to 150 Hz by 10 Hz increments. The power supply voltage for control module was set to 9 and 10 V, respectively. The

module was programmed to a chosen excitation frequency and for each duty cycle setting, amplitude of positive half-cycle V^+ , of negative half-cycle V^- and power supply current I_{CC} were measured. **Figure 15** shows the degree of signal asymmetry S_{ASIM} as a function of the power supply voltage and duty cycle at excitation frequencies from 70 to 150 Hz. We observed that duty cycle of equalization DC_{eq}^+ at 9 V and 10 V of power supply voltage ranged between 30 and 38% and between 40 and 43%, respectively.

Figure 16 shows the driving signal amplitude as a function of duty cycle DC^+ , frequency f ranging from 70 to 150 Hz and power supply voltages of 9 and 10 V. From **Figure 16**, it follows that the maximum amplitude (120 to 130 V) is achieved only in the interval up to 100 Hz (curves 125 and 120 in **Figure 16**, left), while this limit moves up to 110 Hz at higher power supply voltage (10 V, curves 130, 125 and 120 in

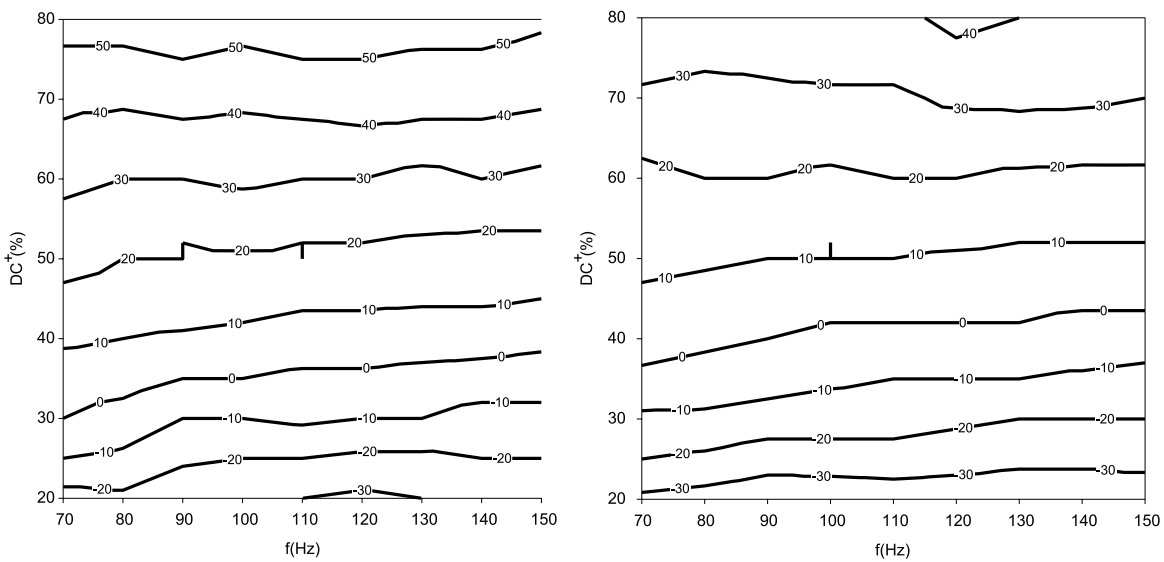


Figure 15. The degree of signal asymmetry S_{ASIM} as a function of duty cycle DC^+ at excitation frequencies f ranging from 70 to 150 Hz at 9 V (left) and 10 V (right) power supply voltage.

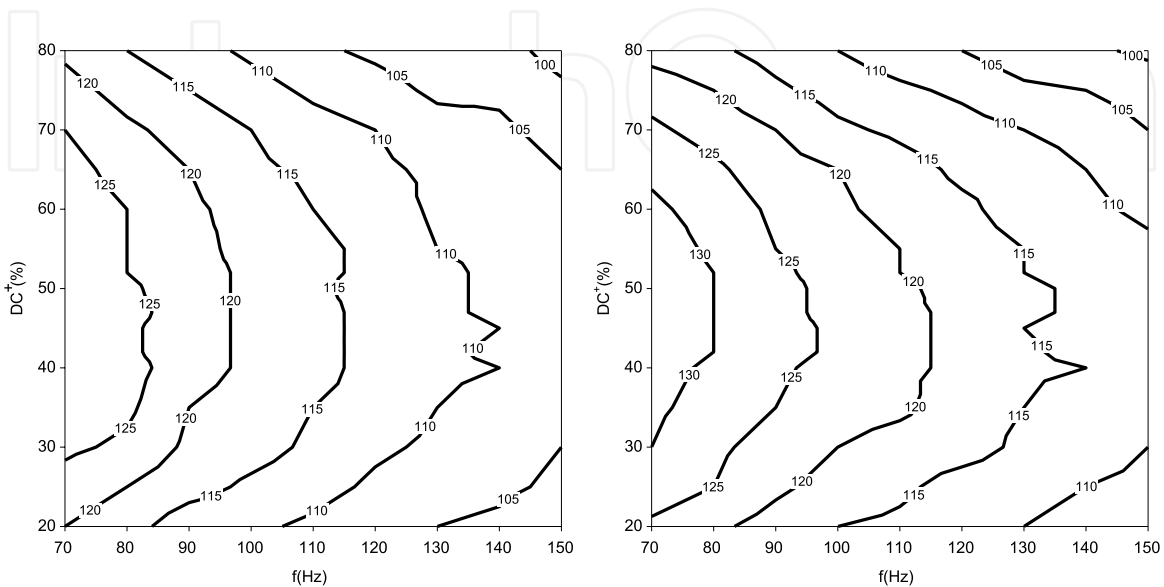


Figure 16. Micropump driving signal amplitude in V as a function of operating frequency and duty cycle DC^+ for power supply voltage of 9 V (left) and 10 V (right).

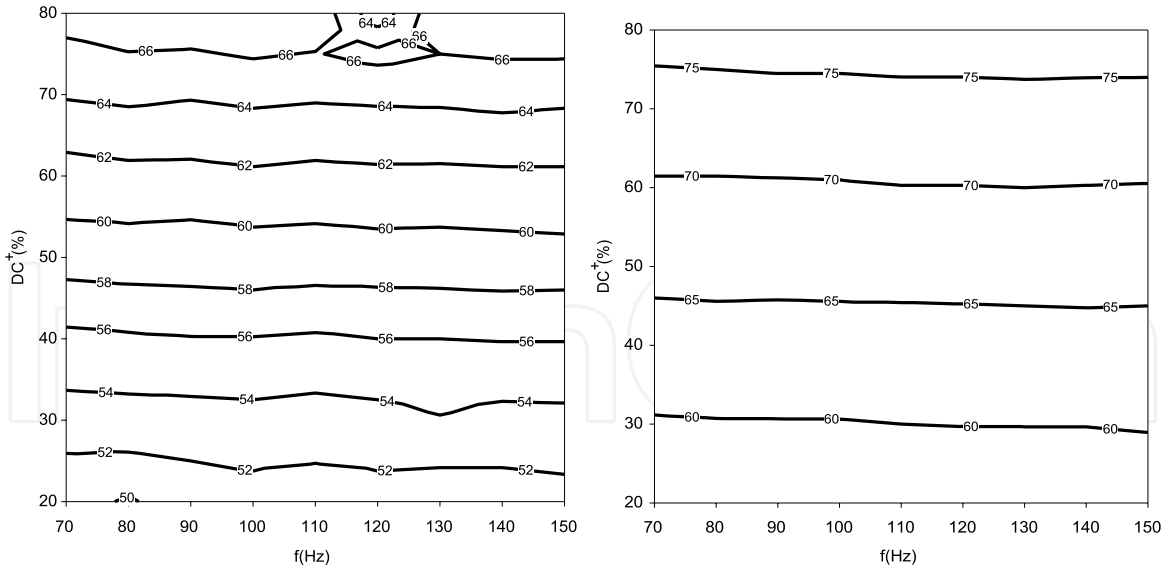


Figure 17. Power supply current in mA as a function of operating frequency and duty cycle DC^+ for power supply voltage of 9 V (left) and 10 V (right).

Figure 16, right). A higher excitation frequency ($\Delta f = +10\%$) affects the flow rate and backpressure performance of piezoelectric micropumps.

Figure 17 shows the power supply current as a function of the power supply voltage and the duty cycle DC^+ at various frequencies ranging from 70 to 150 Hz. From **Figure 17**, it follows that the power supply current is not affected by module operating frequency, which is also supported by the theory of switching power supplies but increases almost linearly with duty cycle DC^+ setting.

The upper limit of duty cycle setting, which keeps the power supply current below 70 mA is 75% and 62% for 9 V and 10 V of power supply voltage, respectively.

Signals of varying degrees of amplitude asymmetry were synthesized by varying the duty cycle setting. Backpressure and flowrate performance of the micropump was shown to be the highest at the duty cycle of equalization $DC_{eq}^+ = 40\%$. To compensate for piezoelectric load and to provide amplitude symmetric driving signal, a solution by fine-tuning of duty cycle setting was proposed.

Duty cycle of equalization DC_{eq}^+ at 9 V power supply voltage ranged between 30 and 38% while at 10 V power supply voltage shifted toward 43%.

3. Optocoupler-based micropump module design

Design, implementation and characterization of a miniaturized piezoelectric micropump driving module, based on two boost SMPS converters, with a shared boost capacitor (micropump PZT actuator) represented a starting point in design of micropump drivers in our Laboratory. This micropump driver design is suitable for integration inside micropump housing due to its small size and its low current consumption (≈ 55 mA).

Such design synthesizes rectangular shape of driving signal with RC charging and discharging transitions, which are not optimal. Low value of both transition slew rates does result in lower current consumption, but at a cost of reduced pump flow rate compared to a steeper slew rate signal. Still, the performance of such a circuit can be considered suitable for certain cost- and size-sensitive applications.

Fluidic measurements have shown the need for assuring driving signal symmetry (i.e. elimination of difference between positive and negative amplitude), which has to be trimmed individually to a particular type of piezoelectric actuator, which was another drawback of this design.

Module upper-frequency limit was found to be at 400 Hz. A typical operation range was found up to 100 Hz, where peak-to-peak amplitudes up to 250 V could be achieved. For DI water pumping, optimal operating frequency range was found between 50 to 80 Hz. Amplitude symmetrical driving signal with an amplitude of 125 V was achieved using power-supply voltage of 9 V, excitation frequency f of 100 Hz and duty cycle DC^+ of 40%. Using these optimal driving conditions considering driving module current consumption and micropump performance characteristics, micropump flowrate performance was found at 0.36 ml min^{-1} , backpressure performance of 104 bar and module power consumption of 0.5 W.

Based on presented fluidic and electrical measurement results, obtained rectangular shape of driving signal with RC charging and discharging transitions, had to be improved to allow faster signal edge transitions (i.e. improved slew rate). Future driver designs also had to allow for a more precise (preferably independent) setting of positive and negative amplitude. Lastly, a wider frequency operation interval than 400 Hz would have to be achieved in order to improve air pumping characteristics.

To implement a driving signal shape of a square wave with settable frequency, duty cycle, both amplitudes and both slew rates, a completely different approach to the design of a miniature high voltage piezoelectric micropump driving module was taken: such design had to synthesize a proper rectangular micropump driving signal with independently settable positive and negative amplitudes, rising and falling edge slew-rates, positive and negative dead-times and excitation frequency.

In order to achieve these functionalities, a simplified high-voltage driving stage was designed. Typical approach would be based on a D-class amplifier design using an isolated gate driver (e.g. STGAP series), which would enable driving piezoelectric micropumps with arbitrary waveforms. On the other hand, such an approach requires several additional components, which would compromise our low-cost approach.

In order to reduce overall cost, the micropump high-voltage switching stage was highly simplified. While isolated gate drivers do provide galvanic isolation between the input section (a microcontroller) and output transistors, they also require a bootstrapping capacitor for high-side switch. Optocouplers perform the necessary level-translation for the high-side transistor and eliminate the need for any additional bootstrap capacitors. Optocoupler-based solution also enables fast transitions and allows for a settable slew-rate as will be presented in the following.

3.1 Module operation

Optocoupler-based design comprises a separate negative and positive high-voltage power supply, each implemented as an independent boost SMPS power supplies, which generate positive and negative micropump driving voltage (**Figure 18**, netlabel V^+ and V^-) from a low voltage source (**Figure 18**, VPWR).

Positive micropump power supply voltage generator is comprised of transistor M1, inductance L1, diode D1 and capacitor C1, while the negative micropump power supply voltage comprises transistor M2, inductance L2, diode D3 and capacitor C3. Both power supply voltage levels (**Figure 18**, netlabel V^+ and V^-) are independently monitored using a dedicated resistor divider (**Figure 18**, resistors R4, R5 and R7, R8 for negative and positive voltage, respectively). Each resistor divider forms a

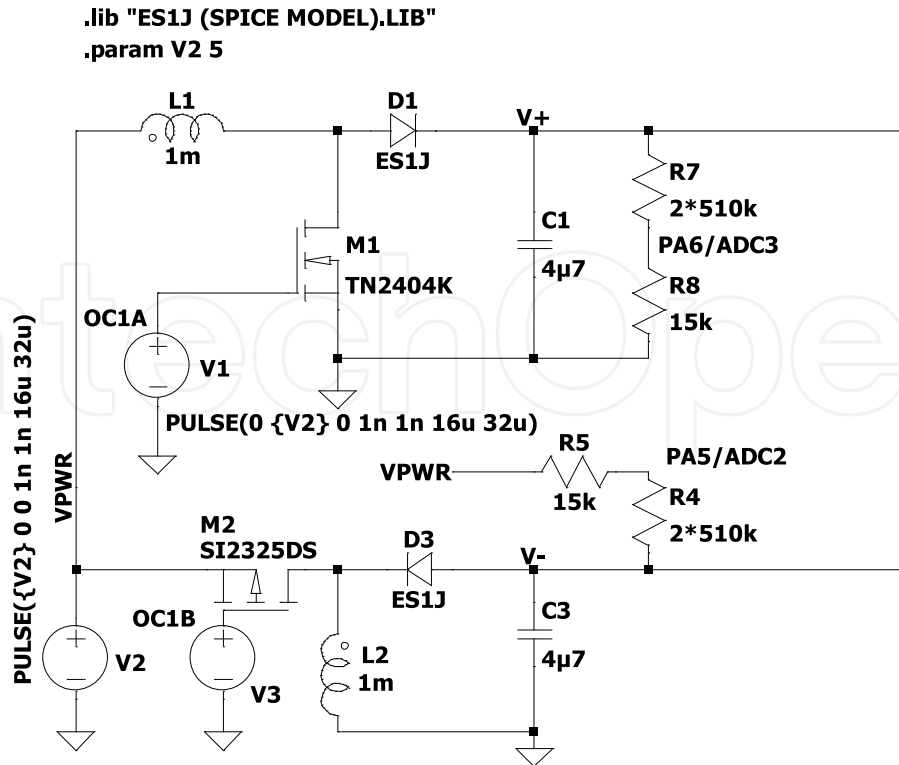


Figure 18.
High-voltage part of the optocoupler-based driver design.

closed-loop voltage regulator with a corresponding microcontroller PWM source (**Figure 18**, labels V3 and V1 for negative and positive voltage, respectively).

Both SMPS converters are driven using PWM signals on sources V1 and V2 (**Figure 18**) with a base frequency of 32 kHz. Achievable duty cycle range is from 10–90%. Depending on duty cycle setting, both SMPS converters can independently deliver output voltage in a range from ± 10 V to ± 150 V. Independent setting of both positive and negative power supply voltage allows the synthesis of a 50% time-symmetrical signal. This could not be achieved using previously presented design, where amplitude symmetry could only be achieved by adjusting the duty cycle of micropump excitation period.

High-voltage switching stage comprises two Darlington output high-voltage optocouplers Toshiba TLP187 (**Figure 19**, circuit U1 and U2). Positive power supply voltage (**Figure 18**, label V^+) is connected to positive voltage switching optocoupler (**Figure 19**, circuit U1), while the negative power supply voltage (**Figure 18**, label V^-) is connected to negative voltage switching optocoupler (**Figure 19**, circuit U2). Independent setting of both power supply voltages and opening of positive and negative voltage optocoupler enable independent setting of rising and falling edge of driving signal as well as positive/negative duty cycle and consequently excitation frequency. Such independent driving introduces an additional part of micropump operating positive/negative half-cycle, called positive/negative dead time, during which both optocouplers are turned off.

In **Figure 19**, only resistors SR1 and SR2 are shown to limit complexity, but more microcontroller output pins may be connected to optocoupler diode input, each via its different value resistor. Using such a setup, a simple D/A (digital-to-analog) converter is formed, which can be used for digitally setting the value of rising/falling edge slew-rate. To enable more fine setting of both slew rates, a microcontroller with an onboard D/A could be used.

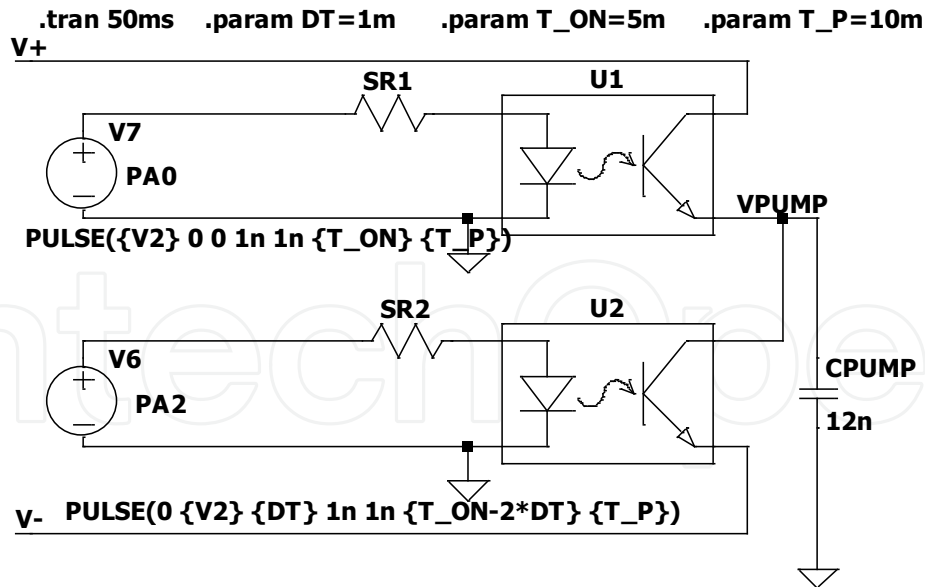


Figure 19.
 Excitation part of the optocoupler-based driver design.

Rectangular micropump excitation signal is synthesized by providing phase-synchronized optocoupler driving signals V6 and V7 (see **Figure 19**, **Figure 20**). Both driving signals must include a programmable dead-time gap, which is downwards limited by optocoupler turn-off-time (80 μ s for TLP187). Any further reduction of this minimal dead-time gap value would shorten out both power supplies.

The micropump switching period is divided into four stages as follows: Positive driving micropump voltage stage, noted by a solid line in **Figure 20**, where positive power supply (**Figure 18**) is connected to the micropump via optocoupler U1 (**Figure 19**). Subsequently, a positive dead time state is next, where both optocouplers are turned off. Following positive dead-time stage, there is a negative driving micropump voltage stage, noted by a dashed line in **Figure 20**. During this stage, negative SMPS power supply (**Figure 18**) is connected to the micropump using

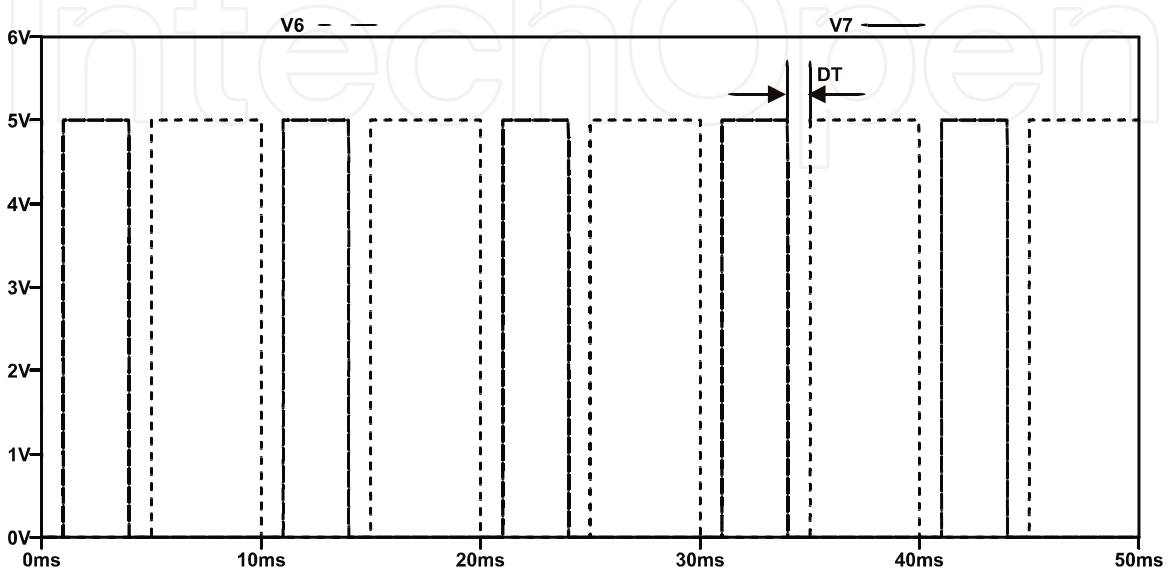


Figure 20.
 Optocoupler diode driving voltage.

optocoupler U2 (**Figure 19**). Micropump excitation period finishes with a negative dead-time stage, where both optocouplers (U1, U2) are again switched off.

Such division of micropump excitation period into four independent stages yields maximum control over micropump driving signal parameters and overall current consumption. Decreasing the value of optocoupler based resistors SR1, SR2 (**Figure 19**) results in higher micropump driving signal slew rates. Selection of resistors represents a compromise between high-flow performance, which is achieved by fast slew-rate and consequentially higher current consumption, and low-flow performance, which is achieved by lower slew-rate and lower current consumption.

Adjusting optocoupler base current using a simplified D/A converter by connecting different resistors enables seamless interchanging between performance modes and different driving signal shapes: Sinus-flank signal (sinusoidal waveform with prolonged flat maximum/minimum) can be obtained by setting both rising and falling slew-rate low using a single, high-value resistor is fed to optocoupler diode. Rectangular signal can be synthesized by setting both slew rates high by turning on multiple resistors. Sinewave-rectangular signal (SRS signal) can be obtained by setting rising edge slew-rate high and falling edge slew-rate low.

Setting of both power supply voltages, slew-rates and dead time preferably have to be implemented in software, using an 8-bit microcontroller. In our cost-effective implementation, depicted in **Figure 6**, a Microchip ATtiny104 [16], was selected for its price and availability in a 14-pin SO package. An 8-bit timer zero is used both for counting through four distinctive signal stages and two-channel PWM synthesis for high-voltage generation. Timer zero is counting using an internal 8 MHz oscillator with no Prescaler, which produces two independent (non-aligned) channel (A and B) 8-bit PWM outputs running at 31.25 kHz. Each PWM channel features a corresponding output compare register (OCR0A/OCR0B).

Driving waveform state machine is stepping through active and dead-time stages for positive/negative amplitudes. Transition to the next state is achieved by presetting timer zero expiration period. After this period, timer zero overflow interrupt causes transition to next state and renewed calculation of next-stage period. Waveform transition state machine can be omitted entirely – in this case, constant positive or negative power supply voltage is connected to the micropump, effectively turning the micropump into a valve.

PWM output (OC0A/OC0B) value results from comparison between OCR0x and timer zero value. These PWM outputs are connected to the corresponding switching transistor (M1, M2 in **Figure 18**). The output (V^+ , V^- in **Figure 18**) of positive/negative power supply SMPS is being monitored using a resistor divider, which is connected to corresponding microcontroller analogue-to-digital converter (ADC) input (ADC2/ADC3, **Figure 18**). An ADC conversion complete interrupt is enabled by timer zero interrupt routine only during positive and negative dead-time switching phase. During positive dead-time state, ADC2 is monitored, and the value of OCR0A is changed accordingly. During negative dead-time state, ADC3 is sampled, and the value of OCR0B is changed. Both positive/negative monitoring algorithms are based on a fast proportional regulator. Microcontroller UART receiver was used to configure all micropump driving signal parameters: frequency, positive and negative amplitudes, dead times, slew-rates and operation type (pumping/valve). In order to reduce the burden of calculations on a microcontroller side, an Excel VBA based script was developed. This script translates human-readable parameters such as frequency and dead time to timer zero state-machine expiration periods, determines slew-rate resistor multiplexing state and configures the mode of module operation.

Switching optocouplers PC817 (U1, U2 in **Figure 19**), which were used during simulations, were replaced with high-voltage, Darlington output type (Toshiba TLP187), due to better switching characteristics and high-current transfer ratio, which achieves higher slew rates. Large (10 $\mu\text{F}/100\text{ V}$) rectifying capacitors (C1, C3 in **Figure 18**) were initially used to minimize the power supply ripple. Their size was reduced during the following measurements.

A digital storage oscilloscope was connected to the driving module prototype. Tested module was driving the micropump with PZT capacitance 12 nF, developed in our laboratory [7]. Developed module can set output signal dead time, between two extrema:

1. Micropump driving voltage is applied almost for the entire corresponding half-cycle, except for dead time, which is set to $DT = 200\ \mu\text{s}$. This is called full drive operating mode. **Figure 21** depicts the front-edge transition of micropump output signal during full drive operating mode at 100 Hz and 100 V. Achieved micropump power supply amplitudes were $\pm 98\text{ V}$.
2. Micropump driving voltage is applied *only* 200 μs of driving time for entire corresponding half-cycle, otherwise signal remains inactive. This is called minimum drive operating mode. Note, that the dead-time (DT) during minimum drive operating mode is depending on the driving signal period ($DT = T/2 - 200\ \mu\text{s}$). Typical dead time clamping value of 200 μs was selected to allow correct optocoupler switching and microcontroller ADC conversions.

Micropump output signal of initial prototype during minimum drive of 200 μs with driving frequency 100 Hz and amplitude $\pm 100\text{ V}$ is shown in **Figure 22**. Piezoelectric

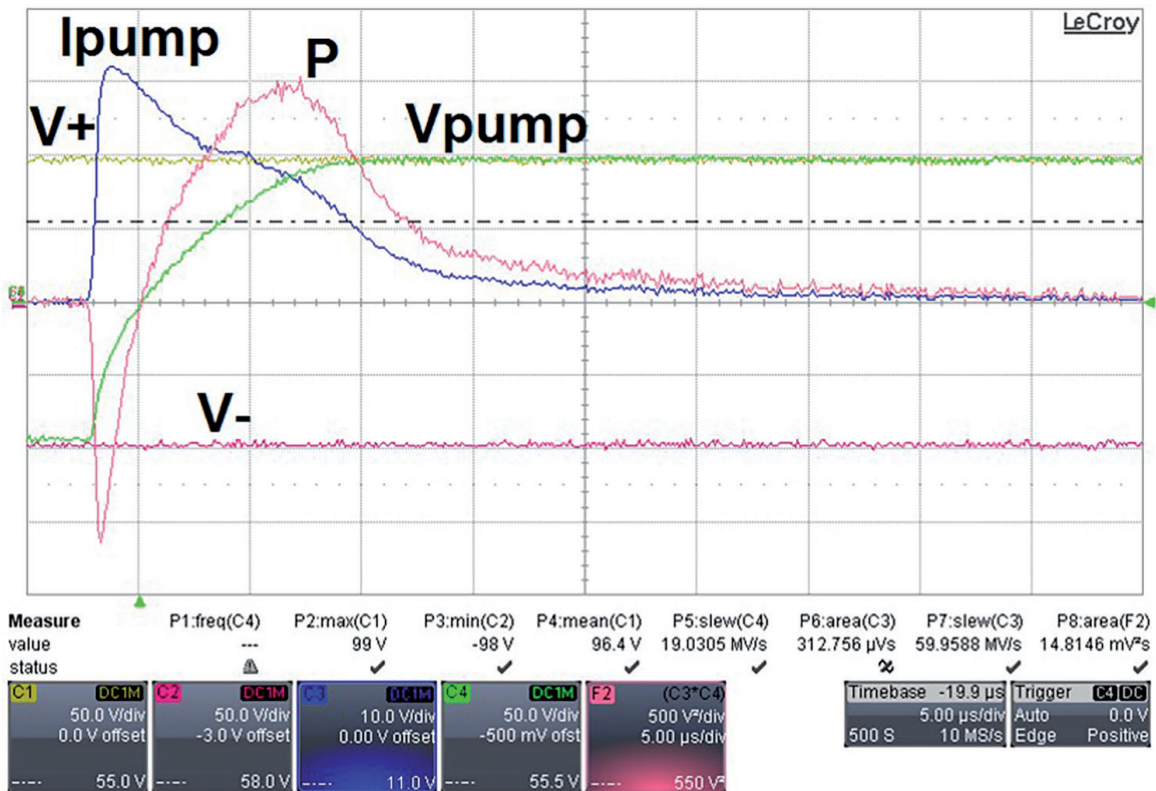


Figure 21.
Initial prototype full drive operation mode front edge detail.

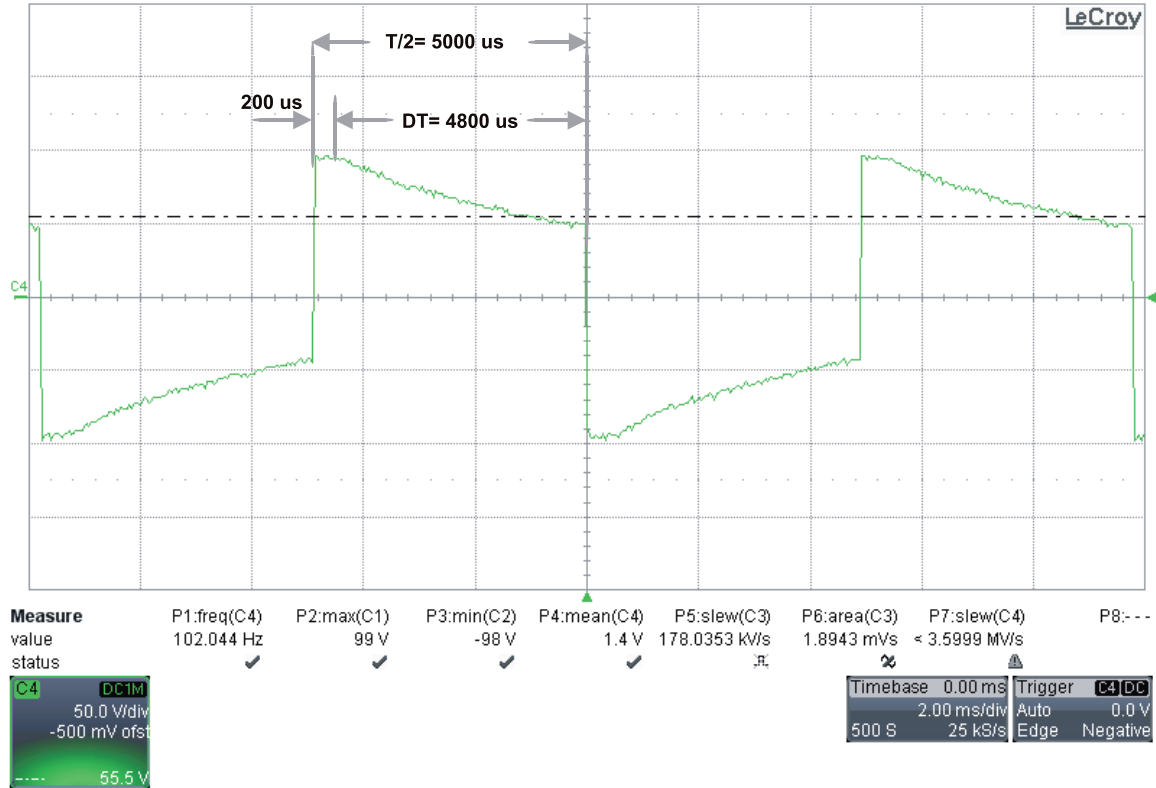


Figure 22.
Initial prototype minimum drive operation mode micropump driving signal.

actuator voltage falls off according to capacitive discharge down to 50 V after initial driving with amplitude ± 98 V for 200 μs (max/min section, **Figure 22**). The time constant of capacitive discharge decay is practically independent of voltage polarity, on the other hand, its value changes depending on pumped media viscosity and micropump design.

3.2 Electrical characterization

Driving signal frequency was investigated in range of 50 Hz to 1 kHz for full and minimum drive operating modes. Micropump driver was configured with maximum piezoelectric actuator voltage of 125 V using Excel control software. Maximum actuator voltage is limited by a maximum field of 600 V/mm of piezoelectric actuator P-5H (Sunnytec Suzhou Electronics Co., Ltd. [13]). Current consumption, positive and negative power supply amplitudes, slew rates and were measured at each micropump frequency value. **Figure 23** is presenting obtained results for micropump amplitude at each excitation frequency setting.

Micropump driver was able to reach admissible voltage limit of ± 125 V in the frequency range up to 150 Hz, which extended initial clamping interval of 70 Hz, achieved with voltage scan of the initial prototype. This extension consequentially increases module current consumption I_{CC} , which is presented in **Figure 24**.

At the target operating frequency of 100 Hz, in full drive operating mode with $SR^+ = SR^- = 16$ V/ μs (**Figure 25**), module current consumption was clamped to 118 mA, at 150 Hz the current consumption increases to 180 mA. In minimum drive operating mode, current consumption reaches 170 mA. Difference in current consumption between ‘full’ and ‘minimum’ driving mode is minimal (10 mA), therefore, the majority of current consumption is attributed to decrease in efficiency of SMPS

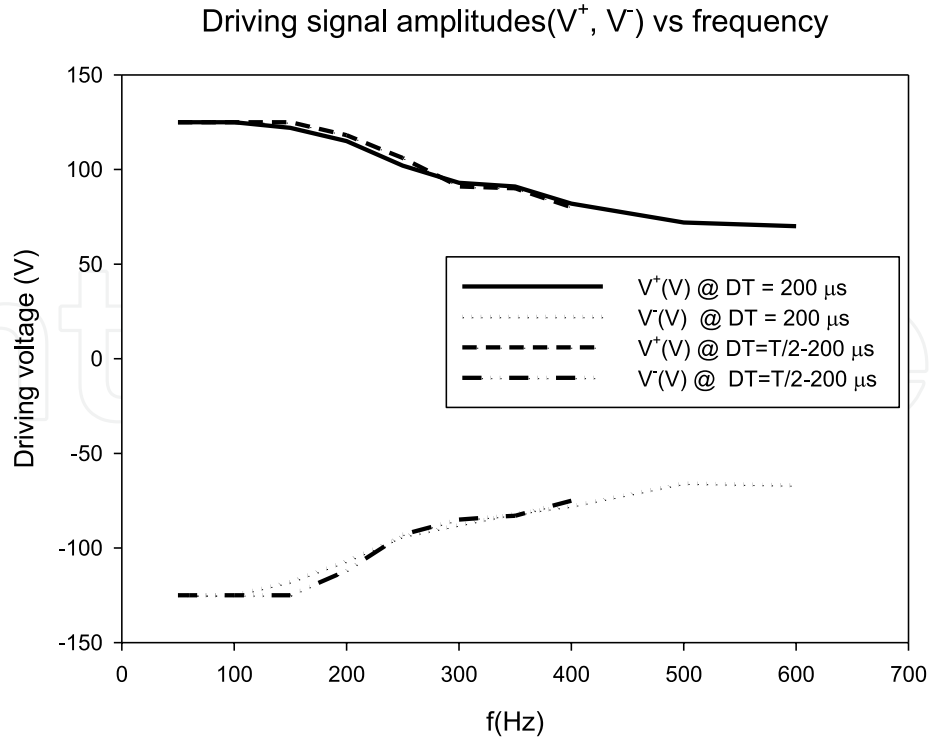


Figure 23.
 Voltage-frequency sweep.

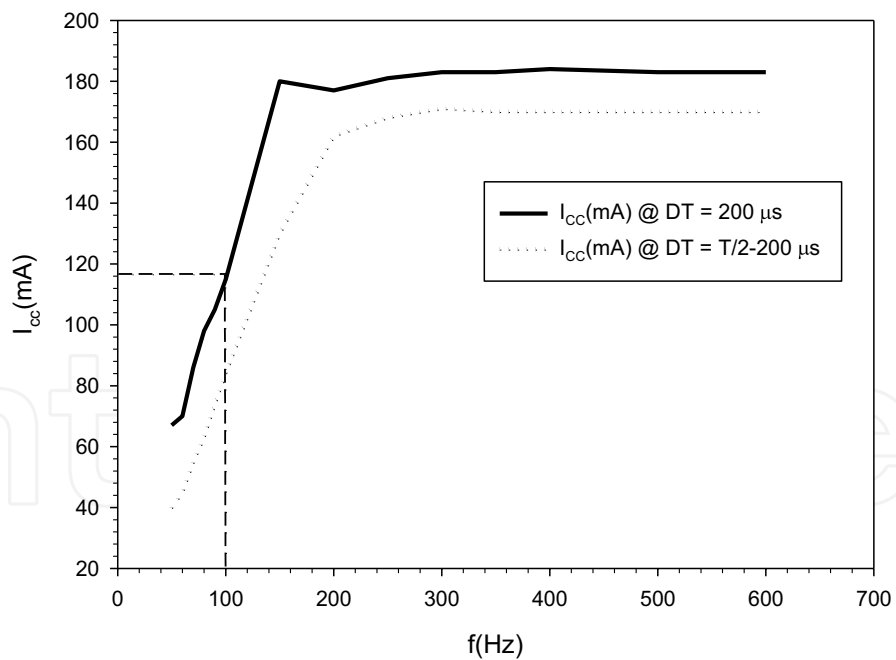


Figure 24.
 Current consumption vs. frequency.

boost converters, when trying to supply actual current to the micropump actuator at such maximum admissible voltage setting. SMPS boost converter current is primarily limited by current capabilities of the used SRR0603 inductor. Current limit value of 180 mA could only be extended by raising the power supply value from 9 V to 10.5 V further to 200 mA for a short period of operation.

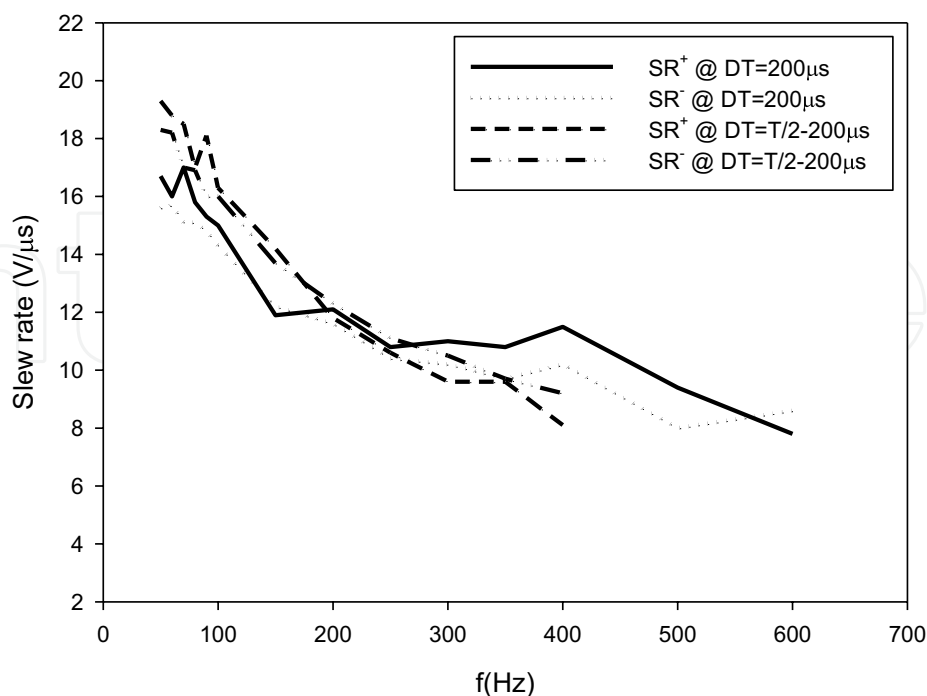
Positive and negative slew rates SR(V/ μ s) vs frequency

Figure 25.
Positive and negative slew rate vs. frequency.

Extension of frequency interval up to 150 Hz (**Figure 23**) with operation at maximum driving amplitude of ± 125 V, resulted in elevation of both slew rates from initial 11 V/ μ s to 16 V/ μ s, when configured to full drive operating mode at 100 Hz, as depicted in **Figure 21**. In minimum drive operating mode, this value is even higher (18 V/ μ s). Slew rate remains well over 10 V/ μ s in the frequency range to 400 Hz, which enables evaluation of our micropumps, with a smaller ($\Phi = 6$ mm) piezoelectric actuator disc with a capacitance of 4 nF [15].

Next, module current consumption was evaluated against slew rate in the full drive operating mode, with micropump excitation frequency of 100 Hz and amplitudes ± 125 V. Measured module current consumption was 118 mA, with both slew-rates set to 16 V/ μ s, shown as a dashed line **Figure 21**.

Waveform measurements, such as frequency, amplitude, both slew rates and waveform averaging were evaluated instantaneously by the oscilloscope. Microcontroller I/O port output driving capability limited any further lowering of optocoupler base resistance to 220 Ω . On the other hand, high limit of optocoupler base resistance was defined by driving signal shape change – driving signal waveform would become sinus-flank if slew-rate values fell below 1 V/ μ s. Current consumption in full drive operating mode (**Figure 24**) remains practically a constant value of 125 mA, independent of slew-rate practically to the limit, where the slew-rate drops to 1 V/ μ s. Average current measurements at high slew rates are hard to establish due to slow data processing of the oscilloscope. In such conditions, the SMPS duty cycle is constantly changing, therefore, any increase in current consumption measurements in full drive operating mode have to be attributed to measurement error. Such measurement errors could be mitigated using a larger output capacitor (**Figure 18**, C1 and C3).

When comparing both operation modes, the majority of current consumption can be attributed to SMPS power sources. In minimum drive operation mode, current

consumption is reduced to 70 mA. Such minimum drive operation mode consequently enables power-saving features during operation with reduced flow. On the other hand, full drive operation mode with its high slew rate improves the micropump air pumping capability, although, for efficient air pumping, driving frequency remains the main limitation factor.

Next, we performed the same set of measurements on a micropump, which comprises a smaller piezoelectric disc with a diameter of 6 mm and a capacitance of 4 nF [15]. Compared to the previously described 12 nF micropump, the clamping voltage (± 125 V) regulation area extended from 150 Hz to 400 Hz. Both slew rates in full drive operation mode achieved levels of 22 V/ μ s, compared to previously achieved 16 V/ μ s. As expected, the current consumption in both modes reduced marginally – compared to values from **Figure 24**, —175 mA in full drive operation mode (previously 180 mA) and 160 mA in minimum drive operation mode (previously 170 mA).

3.3 Fluidic characterization

After the micropump driver testing, the system for computer-controlled characterization of piezoelectric micropumps was set up. Analyzed driving module was connected to tested micropumps, developed in our laboratory [7, 15] using the measurement setup, described in **Figure 10**. Presented micropump driving module was compared to previous driving modules, designed in our Laboratory.

Three distinct micropump designs (N, R, S), each with different outlet channel geometry, were compared using RC asymmetric/symmetric driver and both initial and final versions of the optocoupler based driver. Airflow rate and DI water flow rate measurements were performed at 100 Hz, while the presented driver was configured in full-drive operation mode in both initial and optimized versions.

Achieved air flow rate with a symmetric RC driver was 1.6 sccm. This value increased to 4.2 sccm with optocoupler based driver in full-drive operation mode. Compared with symmetric and asymmetric versions of RC driver, presented driver surpasses all previous performances. Achieved DI water flow rate with a symmetric RC waveform-like driver was 2.2 sccm. This value was increased to 2.6 sccm with optocoupler based driver in full-drive operation mode. Achieved air backpressure performance almost doubled with the use of optocoupler based driver: It is achieving its peak value of 39 mbar on N1 type micropump in ‘full drive’ mode. Achieved DI water backpressure performance improved by 30%, compared to initial version of RC waveform-like driver: It is achieving its peak value of 240 mbar on N1 type micropump in “full drive” mode. Both presented versions improved DI water backpressure performance over RC waveform-like drivers.

Optocoupler based driver was set up at 100 Hz with ± 105 V amplitudes in full drive operation mode a micropump S29R1 was connected to its output. Slew-rate values were altered in the range from 0.2 V/ μ s to 16 V/ μ s, while both DI water and airflow rates were measured. In both cases, the flow rate is practically independent of the slew-rate (**Figure 26**).

Figure 28 is showing a slight decrease in backpressure characteristics with decreasing slew rate SR^+ . This performance deteriorates severely when the slew rate falls below 4 V/ μ s. If slew rate is lowered even further down to 1 V/ μ s, comparable conditions as in the case of RC waveform-like driver may be achieved with reduced current consumption to 100 mA (see **Figure 27**) at 5 V module power supply. Even with slew rate kept as low as 1 V/ μ s, resulting flow rate is significantly higher

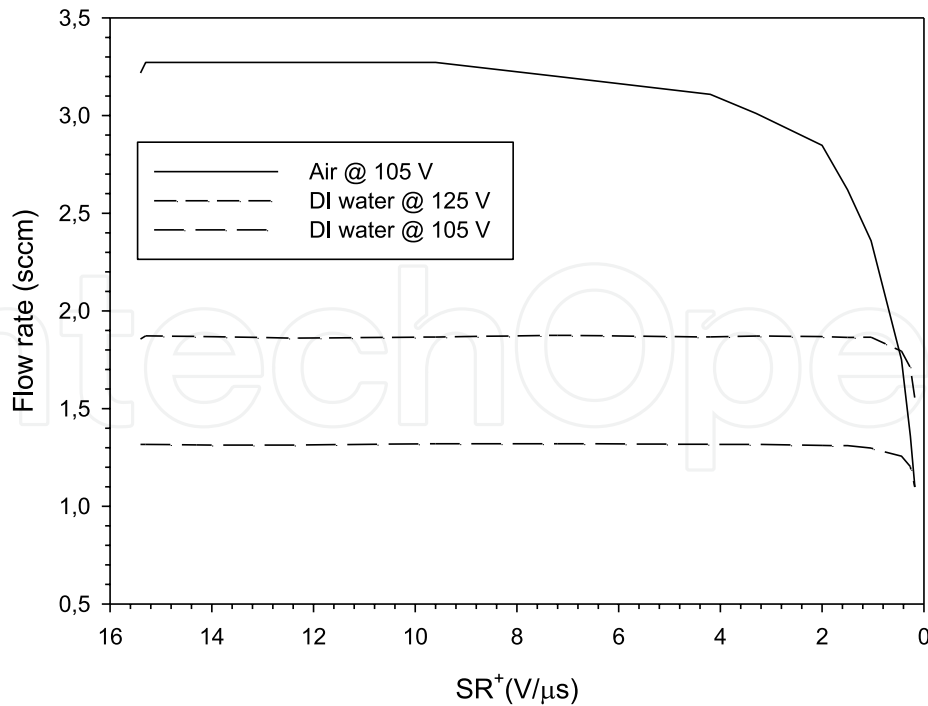


Figure 26.
Air, DI-water flow rate vs. slew rate in “full drive” mode.

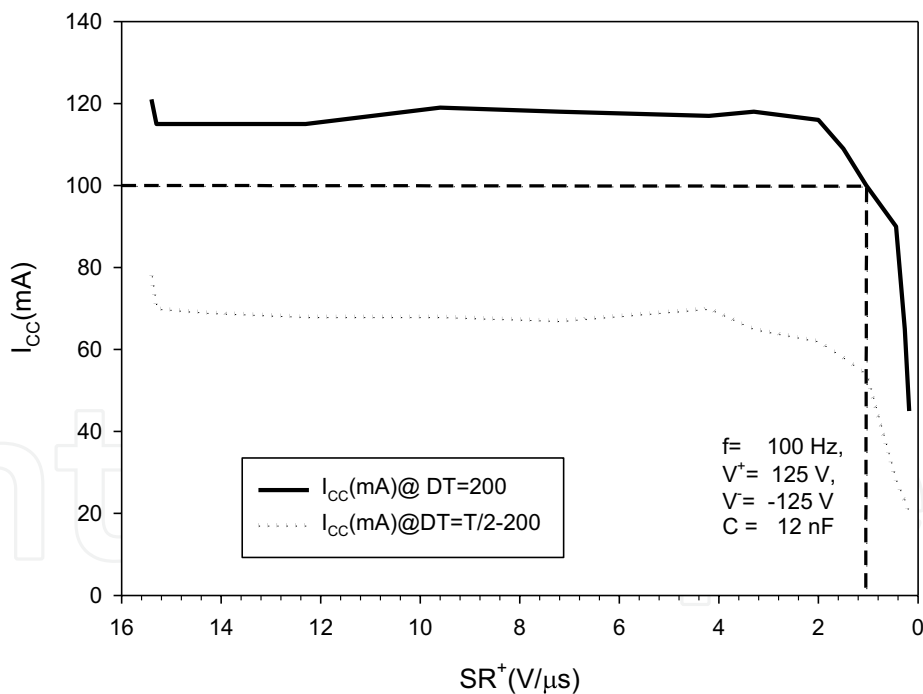


Figure 27.
Current consumption vs. positive slew-rate.

compared to our RC driving module versions, which achieved slew rates of $0.2 \text{ V}/\mu\text{s}$. Current consumption can be further reduced using minimum drive operation mode.

Starting values of SR^+ in **Figure 28** indicate that high slew rates at $16 \text{ V}/\mu\text{s}$ have only a minor impact on flow rate and backpressure characteristics at a significantly higher current consumption. However, higher slew rates improve/stabilize other micropump properties and such as self-priming and bubble tolerance and enable a more reliable micropump operation in different operating conditions.

Backpressure vs. slew-rate @ 106V

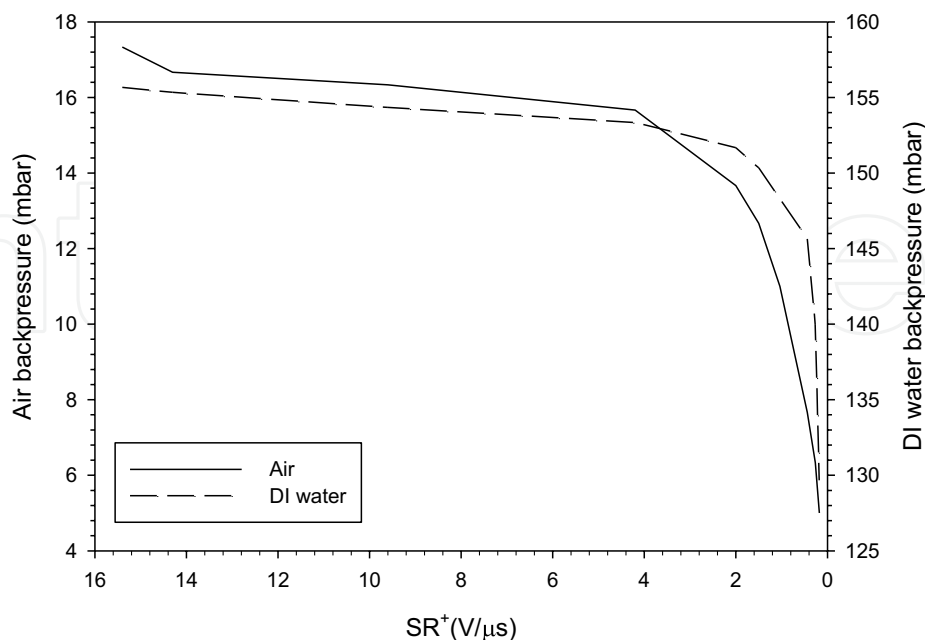


Figure 28.
Air, DI-water backpressure vs. slew-rate in “full drive” mode.

4. Miniaturized arbitrary-waveform generator design

Advanced piezoelectric micropump driver, designed as a miniaturized arbitrary waveform generator for driving custom made piezoelectric micropumps represents a large leap from initial capacitive charging/discharging square-wave shape: Developed driver enables independent setting of several output signal parameters, such as frequency, both positive/negative amplitude, both slew-rates, dead time, and modes of operation (pump/valve). Compared to optocoupler based design, dead time and slew rates are made a part of synthesized waveform and are therefore software settable in far more refined form than using resistor based D/A converter.

Air pumping characteristics of micropumps, manufactured in our laboratory, exhibited no distinct frequency peak in backpressure and flow performance. This result led to the development of a different driver, which would elevate driving frequency in order of several kHz. While the square-wave signal offered best flow and backpressure results, it also induces excessive stress on piezoelectric actuator, which might reduce its lifetime, therefore the need for other shapes of driving waveforms was established. Driving of micropumps with other signal types (e.g. sinewave), results in reduced stress on micropump piezoelectric actuator and also reduces current consumption at higher driving frequencies. Based on the previous designs, we concluded that the arbitrary waveform driver output stage should feature separate high-voltage boost stages, which are able to independently set micropump positive and negative supply voltage. Furthermore, in order to efficiently boost arbitrary micropump driving signals, a full amplification stage, based on an operational amplifier, similar to [17, 18] had to be designed instead of previously proposed interchanging boosting stages or simplified optocoupler-based square wave stage. Generating a micropump driving voltage using PWM approach has proven too slow for synthesis of driving signals above 400 Hz, therefore development in direction

of D class amplifier was abandoned. Designed piezoelectric driving module would have to be capable of synthesis of arbitrary signals from DC to several kHz if we want to cover pumping of both liquids and gases. It should apply 32 kHz PWM frequency on two separate high-voltage power supplies to achieve amplitudes up to 150 V_{PP} using 5 V power supply voltage. The module parameters such as micropump excitation voltage, frequency and symmetry should be programmed using a PC. Module itself is USB powered and is to be designed with size-sensitive applications aspect. In addition to microfluidic applications, the module versatility can be extended to the evaluation of arbitrary piezo actuators in microsystems or advanced haptics.

4.1 Module operation

The concept of a separate, independently settable high voltage power supply section was already successfully implemented with the previously presented optocoupler based driver. During current consumption measurements, it was demonstrated, that the reduction of voltage step-up ratio significantly improves current driving capabilities of output stage. This design uses the same topology, capable of boosting the micropump power supply voltage in a range from ± 10 V to ± 150 V, depending on duty cycle setting (**Figure 18**, node label V^+ and V^-). Both SMPS converters are driven using PWM signal (**Figure 18**, sources V1 and V2) with PWM frequency 32 kHz in range from 10–80%. Additional low-voltage boost SMPS, which generates +10 V from a single +5 V power supply was added to reduce the voltage step-up ratio. Independent setting of power supply voltage levels allows adjustment of amplitude symmetry by separately adjusting the signal waveform and signal DC offset. Both high-voltage power supply outputs (**Figure 18**, V^+ and V^-) are connected to the operational amplifier high voltage power supply inputs (**Figure 29**, V^+ and V^-). High voltage boost stage comprises a single operational amplifier (U1), which feeds two common base transistor amplifiers. Positive output voltage common base amplifier (Q4 and R3) is used to translate low-output operational amplifier voltage (VAMPOUT) through R1 current onto base resistor R3, which opens positive voltage output driver Q2. Similarly, for negative output voltages, the common base amplifier (Q3 and R2) opens negative output voltage driver Q1. Note, that operation of this stage is inverting i.e. a negative swing of potential VAMPOUT causes a positive swing of output voltage VOUT. Operation of high voltage boost stage is controlled using a negative feedback loop, comprised of resistors RF1, RF2 and a capacitor C3 for frequency compensation.

Due to inverting nature of output stage, a *non-inverting input* of operational amplifier is used to complete the loop. Such feedback implements an overall non-inverting high voltage amplifier with amplification of $A_U = 42.6$, which is able to amplify input amplitude of $VAMPIN = \pm 3.3$ V to output voltage range $VOUT = \pm 140$ V.

Selection of C3 at 470 pF limits input signal (VAMPIN) bandwidth to approximately 10 kHz, a decade above frequency limits, achieved with previous versions of our driver (max. 900 Hz). Minor drawback of presented non-inverting high voltage amplifier stage is the polarity of input signal VAMPIN: In order to achieve full output voltage swing, input signal also needs to be bipolar, which is inappropriate for driving with a microcontroller fed from a single 3.3 V power supply.

To be able to use unipolar input driving signals, a separate transformation stage, depicted in **Figure 30**, was designed. Operational amplifier U2 forms a voltage subtractor, which produces an output voltage (VAMPIN) as an amplified difference

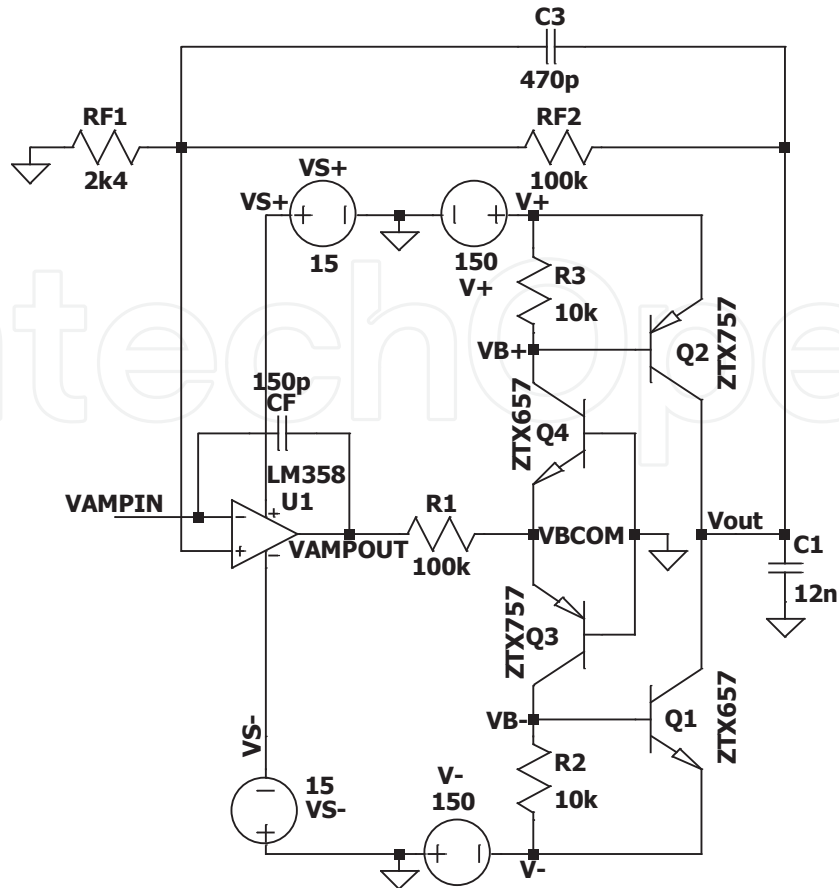


Figure 29.
 Non-inverting high voltage amplifier stage.

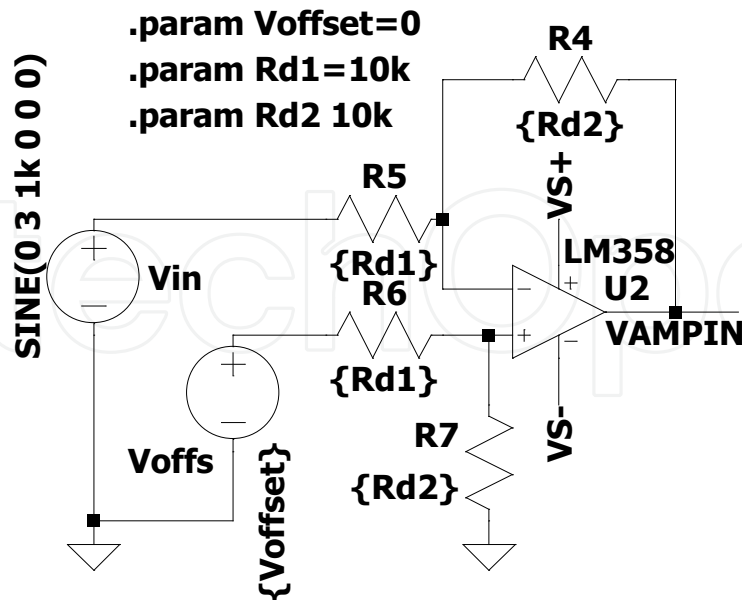


Figure 30.
 Signal conditioning part of the driver.

between signal input (V_{in}) and offset input (V_{offs}). Current selection of feedback resistors $R_5 \dots R_7$ values R_{d1} , R_{d2} ratio results in amplification of $A_U = 1$.

Micropump control is achieved using a cost-effective (5€/unit) 32-bit ARM Cortex 4 microcontroller, an STM32G431KB in LQFP-48 package [19]. Selected microcontroller

also features 16-bit timer (TMR2), which in combination with 12-bit buffered digital-to-analog converter (DAC1) and a 12 channel direct-memory-access (DMA) controller forms a direct digital synthesis system (DDS), capable of synthesizing digital signals with update rate of 1 MSPS. Important fact is that the DDS entirely bypasses the microcontroller core, thus saving time for additional tasks, such as communication and PWM regulation for operational amplifier power supply (**Figure 18**, VS1, VS2) and high-voltage supply voltage (V^+ and V^-) channel PWM. Selected microcontroller also features two separate 16-bit analog-to-digital converter units (ADC).

Each PWM controller uses a dedicated ADC channel in combination with one of PWM channels, available in timer (TMR1). ADC interrupt is triggered whenever conversion is complete on all four selected channels, afterwards PWM is adjusted according to power supply set-point. Microcontroller TMR1 PWM unit channels are configured independently, with four output compare registers (TMR1/CH2 and TMR1/CH3), running at 32 kHz with 12-bit resolution. PWM outputs are connected to the corresponding SMPS transistor (M1, M2 in **Figure 18**) via MOSFET driver TC4427.

Each SMPS output is monitored by feedback to the corresponding microcontroller analogue-to-digital converter input (ADC2/ADC3, **Figure 18**). After DDS generation is configured and started, it operates independently of processor actions. Input characteristic is calculated using voltage subtractor equations (see **Figure 30**) valid for ideal or DC operation, while at higher frequencies, amplification deterioration has to be taken into account. To mitigate this, the driving signal has to be monitored separately and the voltage subtractor input recalculated to actually achieved waveform positive and negative extrema. Microcontroller USB-CDC receiver was utilized as a communication interface for adjustment of all micropump driving signal parameters.

4.2 Electrical characterization

Micropump piezoelectric actuator excitation voltage was limited to ± 125 V due to PZT actuator electrical field limitation and micropump frequency was set from 10 Hz to 9.2 kHz using a sine-wave and square-wave excitation signal. Positive and negative driving signal amplitudes, achieved on the micropump actuator, and current consumption were measured at each micropump frequency setting. Micropump driving voltage amplitudes (V^+ and V^-) vs. excitation frequency results are presented in **Figure 31**.

In the low-frequency range, micropump driving signal clamped out to an admissible voltage limit of ± 125 V, before it begins to deteriorate (**Figure 31**). In comparison to driving voltage vs. frequency scan of our previous prototypes, this clamping interval extended from 150 Hz to 1 kHz. Upper (V^+) and lower (V^-) voltage characteristics in **Figure 31** represent achievable voltage limits, which can be regulated by a voltage monitor.

Such extension of clamped-out driving signal amplitudes consequently results in an increased module current consumption I_{CC} , which is presented in **Figure 32**. Previously developed modules were capable of producing square wave driving signals in frequency range up to 700 Hz and its current consumption reached 118 mA at 100 Hz and 180 mA at 150 Hz.

Current miniaturized arbitrary waveform generator design also offers driving using sine-wave, where the true driving signal frequency extension becomes obvious: It can extend frequency driving interval up to 9.2 kHz. Current consumption using

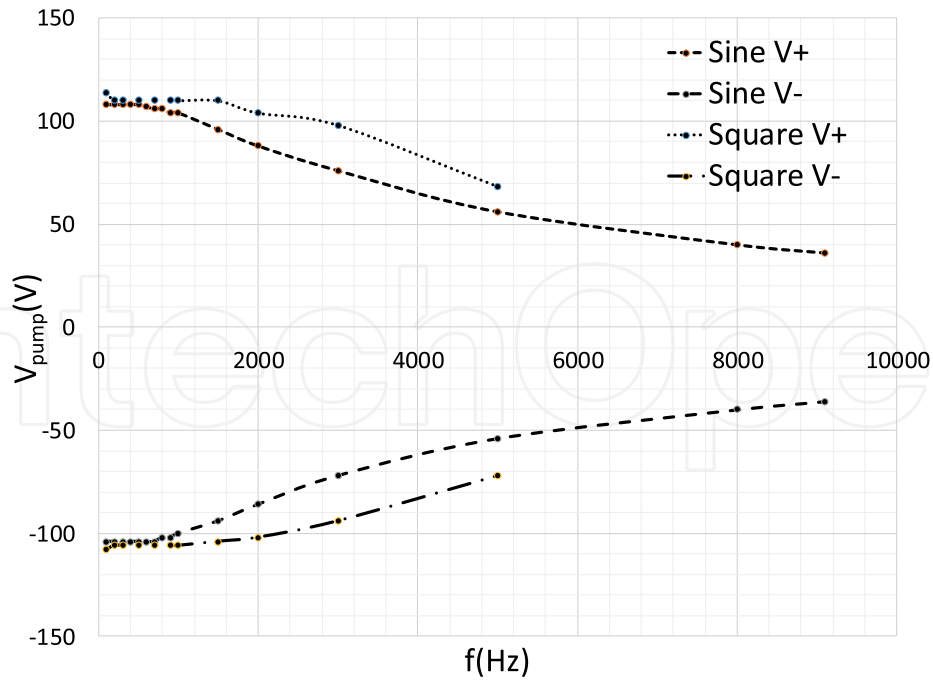


Figure 31.
Voltage -frequency sweep.

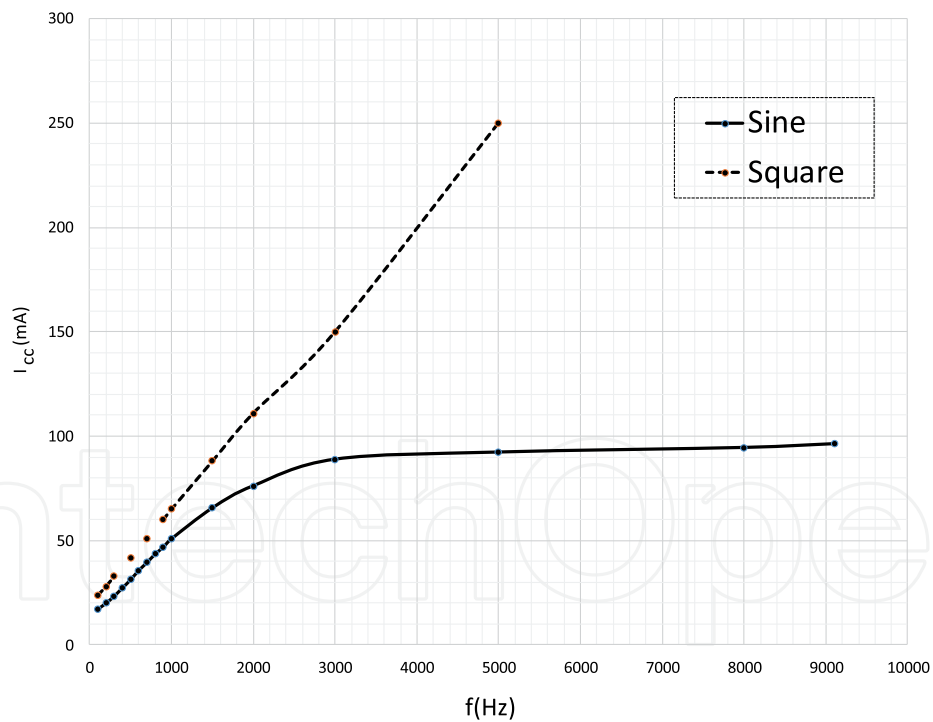


Figure 32.
Current consumption vs. frequency.

square wave driving signal is also reduced: it reaches 40 mA at 100 Hz and 75 mA at 1 kHz. A major improvement, shown in **Figure 32**, is the ability of presented driver to generate a sinewave signal, which results in a far smaller current consumption compared to square-wave driving signal. As shown in our previous research, square-wave signal offer better fluidic performance, while sinewave offer more stable micropump operation with far less stress on piezoelectric actuator.

4.3 Fluidic characterization

After initial electrical testing, fluidic characterization was performed using the same computer controlled characterization system (see **Figure 10**). Analyzed driving module was connected to tested micropumps, developed in our laboratory [7, 15]. Our previous research of micropump performance on signal shape was focused primarily on the optimization of square-wave signal parameters to improve micropump flow and backpressure performance. Impact on the slew-rate increase was demonstrated in the optocoupler based design results.

In the following measurements, we intend to focus on pumping of air, because the presented driver excelled at generating frequencies above 1 kHz, which we were unable to implement on our previous designs. Presented micropump driving module was compared to previously described driving modules, designed in our Laboratory (RC-like rectangular signal driver and optocoupler-based driver). Micropump design S32S2 with small outlet channel geometry was used for comparison between RC symmetric driver and latest version of the presented driver. Air flow rate (**Figure 33**) and DI water flow rate (**Figure 34**) measurements, were performed with sinewave signal in the frequency range from 100 Hz to 3 kHz.

Presented driver performs significantly better than previous RC waveform-like driver, especially in air pumping, where it increases the air flow rate (from 1.6 sccm to 2.2 sccm) in comparison with symmetric-amplitude RC waveform-like driver. Compared with symmetric and asymmetric versions of RC waveform-like driver, presented driver surpasses all previous performances of previously described drivers.

Compared to the optocoupler design, flow rate decrease for DI water from 3.3 ml/min to 2.2 ml/min seems substantial. Note, that 3.3 ml/min was obtained using square-wave signal with higher slew rate on optocouplers. In arbitrary waveform design, such slew rates could not be achieved not even using square-wave measurement. However, presented driver almost doubles air backpressure performance, compared to RC type driver (39 mbar) and is achieving its peak value of 52 mbar on N1 type micropump using sinewave driving signal. The flow rate and backpressure characteristic flatten out at 3 kHz, therefore this represents the usable driving frequency range for tested micropumps.

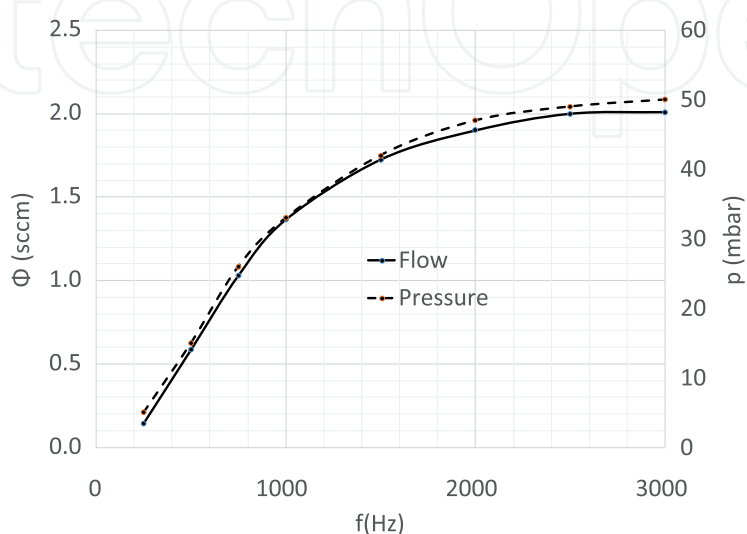


Figure 33.
Air flow rate and backpressure vs. frequency.

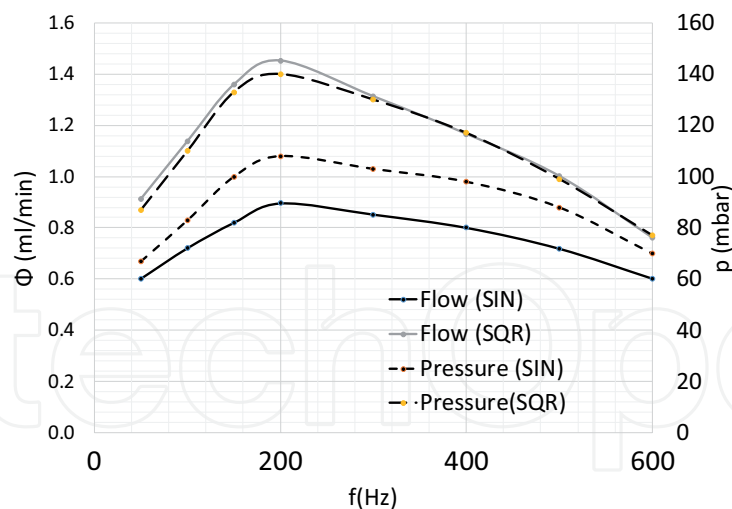


Figure 34.
DI water flow rate and backpressure vs. frequency.

5. Conclusion

Design, implementation and characterization of three distinctive piezoelectric micropump driving module designs were presented.

Our initial design was based on a miniature, transformerless version of a piezoelectric micropump driving module, based on two switched-mode power supply (SMPS) boost converters with a shared SMPS inductance and piezoelectric micropump actuator (as a common output capacitor). Its small size and its low current consumption (≈ 55 mA) make presented driver suitable for integration inside micropump housing, targeting principally cost-sensitive and low-power applications. This module synthesized driving frequencies in the range of 400 Hz while achieving amplitudes up to $250 V_{pp}$ (frequency range up to 80 Hz). Optimal operating frequency range for micropump actuation was found around 50 to 80 Hz during tests using DI water pumping. Optimal driving conditions considering driving module current consumption and micropump performance characteristics (power supply voltage of 9 V, excitation frequency f of 100 Hz and duty cycle DC^+ of 40%) resulted in amplitude symmetric driving signal with an amplitude of 125 V, micropump flowrate performance of 0.36 ml min^{-1} , backpressure performance of 104 mbar and module power consumption of 0.5 W. Unfortunately, this design required a separate mechanism form equalizing discrepancies in positive and negative driving amplitude.

Next, we introduced an optocoupler-based driver design, which achieved higher driving frequencies in range up to 1 kHz and amplitudes up to $250 V_{pp}$ (in lower frequency range up to 150 Hz), making this design optimal for pumping DI water, where positive and negative signal slew-rates up to $18 \text{ V}/\mu\text{s}$ were achieved. In comparison with our previous driver design, this version eliminates the need for equalization of driving signal amplitudes. Furthermore, it increases airflow capability from 1.6 sccm to 3.3 sccm, although the air was not the primary target of pumping media for this design. Maximum module power consumption was 1.6 W (180 mA @ 9 V).

Finally, an arbitrary waveform piezoelectric micropump driver for driving custom made piezoelectric micropumps was presented. Driving signal frequency range from several Hz to 9.2 kHz was investigated and amplitudes up to $125 V_{pp}$ were achieved in the frequency range up to 1 kHz. Optimal micropump actuation frequency of 3 kHz for pumping air was found. Indeed, it does not achieve airflow capability of presented

optocoupler based driver, however, it is capable of achieving almost double (59 mbar) backpressure at reduced current consumption of 500 mW (100 mA @ 5 V) using a sinewave driving signal. Presented modules are capable of driving a 200 μm thick piezoelectric actuator with a capacitance in span from 4 nF to 12 nF.

Acknowledgements

This research was funded by Slovenian Research Agency/ARRS, grant number P2-0244. The authors would like to thank the Slovenian Research Agency and Ministry of Education, Science and Sport for their support of this work.

Conflict of interest

The authors declare no conflict of interest.

Author details


Matej Možek^{1*}, Borut Pečar¹, Drago Resnik^{1,2} and Danilo Vrtačnik¹

1 Laboratory of Microsensor Structures and Electronics (LMSE), Faculty of Electrical Engineering, University of Ljubljana, Ljubljana, Slovenia

2 Chair of Microprocess Engineering and Technology–COMPETE, University of Ljubljana, Ljubljana, Slovenia

*Address all correspondence to: matej.mozek@fe.uni-lj.si

IntechOpen

© 2022 The Author(s). Licensee IntechOpen. This chapter is distributed under the terms of the Creative Commons Attribution License (<http://creativecommons.org/licenses/by/3.0>), which permits unrestricted use, distribution, and reproduction in any medium, provided the original work is properly cited. 

References

- [1] Bartels mp-x Controller. Available from: <https://www.bartels-mikrotechnik.de/elektronik/> [Accessed: November 15, 2021]
- [2] Bartels mp6-OEM Controller. Available from: https://www.bartels-mikrotechnik.de/wp-content/uploads/simple-file-list/EN/Manuals-and-Data-Sheets/mp6_electronics_Datasheet.pdf [Accessed: November 15, 2021]
- [3] Antonijević M, Dolžan T, Pečar B, Aljančič U, Možek M, Vrtačnik D, et al. Characterization System for Piezoelectric Micropumps, 48th International Conference on Microelectronics, Devices and Materials & the Workshop on Ceramic Microsystems, September 19–September 21, 2012, Otočec, Slovenia. Proceedings. Ljubljana: MIDEM - Society for Microelectronics, Electronic Components and Materials. pp. 357-362
- [4] Smole D, Dolžan T, Pečar B, Aljančič U, Možek M, Vrtačnik D, et al. Low-Power Piezoelectric Micropump Driving Module. 50th International Conference on Microelectronics, Devices and Materials, October 8–October 10, 2014. Ljubljana, Slovenia. pp. 139-144
- [5] Baumann T, Hoene E. Highly Miniaturized Piezoactor Drive, Fraunhofer-Institut IZM. Available from: <http://www.powerguru.org/highly-miniaturized-piezoactor-drive/> [Accessed: November 15, 2019]
- [6] LTSPICE4. Linear Technologies. Available from: <http://ltspice.linear-tech.com/software/LTspiceXVII.exe> [Accessed: November 15, 2021]
- [7] Dolžan T, Pečar B, Možek M, Resnik D, Vrtačnik D. Self-priming bubble tolerant microcylinder pump. *Sensors and Actuators A: Physical*. 2015;233:548-556. DOI: 10.1016/j.sna.2015.07.015
- [8] 8-bit AVR Microcontroller: ATtiny4 / ATtiny5 / ATtiny9 / ATtiny10 DATASHEET. Available from: <http://ww1.microchip.com/downloads/en/DeviceDoc/ATtiny4-5-9-10-Data-Sheet-DS40002060A.pdf> [Accessed: November 15, 2021]
- [9] Woias P. Micropumps—Past, progress and future prospects. *Sensors and Actuators B: Chemical*. 2005;105(1):28-38. DOI: 10.1016/j.snb.2004.02.033
- [10] Jeong OC, Konishi S. Fabrication of all PDMS micro pump. In: *IEEE International Symposium on Micro-NanoMechatronics and Human Science*. IEEE; 2005. pp. 139-143. DOI: 10.1109/MHS.2005.1589977
- [11] Guan Y, Ren J, Zhang G, Cheng Z. Fabrication and experiment studies of the piezoelectric micropump with saw-tooth microchannel. In: *IEEE International Conference on Intelligent Computing and Intelligent Systems (Vol. 2)*. IEEE; 2009. pp. 733-737. DOI: 10.1109/ICICISYS.2009.5358282
- [12] Guan YF, Shen MG, Han LL. Simulations and experiment analysis of a piezoelectric micropump. In: *Applied Mechanics and Materials (Vol. 229)*. Trans Tech Publications; 2012. pp. 1688-1692
- [13] Piezoelectric actuator P-5H datasheet Sunnytec Suzhou Electronics Co., Ltd. Available from: <http://sunnytec-piezo.com/en/product.asp> [Accessed: November 15, 2021]
- [14] Pečar B, Možek M, Vrtačnik D. Thermoplastic-PDMS polymer covalent bonding for microfluidic applications. *Informacije MIDEM*. 2017;47(3):147-154

[15] Pečar B, Resnik D, Aljančič U, Vrtačnik D, Možek M, Amon S. Bubble tolerant valveless piezoelectric micropump for liquid and gasses. In: 47th International Conference on Microelectronics, Devices and Materials and the Workshop on Organic Semiconductors, Technologies and Devices, September 28–September 30, 2011, Ajdovščina, Slovenia. Proceedings. Ljubljana: MIDEM - Society for Microelectronics, Electronic Components and Materials; 2011. pp. 57-61

[16] 8-bit AVR Microcontroller ATtiny102 / ATtiny104 Datasheet complete. Available from: http://ww1.microchip.com/downloads/en/devicedoc/atmel-42505-8-bit-avr-microcontrollers-attiny102-attiny104_datasheet.pdf [Accessed: November 15, 2021]

[17] Texas Instruments AN-272 Op Amp Booster Designs. 1981. Available from: <https://www.ti.com/lit/an/snoa600b/snoa600b.pdf> [Accessed: November 15, 2021]

[18] Analog Devices, Power Gain Stages for Monolithic Amplifiers. 1986. Available from: <https://www.analog.com/media/en/technical-documentation/application-notes/an18f.pdf> [Accessed: November 15, 2021]

[19] ST Microelectronics Devices, Mainstream Arm Cortex-M4 MCU 170 MHz with 128 Kbytes of Flash memory, Math Accelerator, Medium Analog level integration. Available from: <https://www.st.com/en/microcontrollers-microprocessors/stm32g431kb.html> [Accessed: November 15, 2021]